LITHOS 466-467 (2024) 107466

Contents lists available at ScienceDirect

LITHOS

journal homepage: www.elsevier.com/locate/lithos

Compositional changes with incremental growth of the Quxu granite batholith, southern Tibet: Evidence from geochronology and geochemistry

Ying-Ze Zhang, Xiao-Lei Wang *, Yue Guan, Xiu-Mian Hu, Jun-Yong Li, De-Hong Du, Di Wang

State Key Laboratory for Mineral Deposits Research, School of Earth Sciences and Engineering, Frontiers Science Center for Critical Earth Material Cycling, Nanjing University, Nanjing 210023, China

ARTICLE INFO

Keywords:
Compositional change
Granite batholith
Incremental growth
Magma recharge
Magma reservoir

ABSTRACT

How to reconstruct the detailed processes and identify the key factors of incremental growth to form a large granite batholith is controversial. Such in-depth investigations along convergent plate boundaries are of great importance for better understanding the growth and reworking of continental crust. This work presents an integrated study of SIMS (secondary ion microscope) U-Pb geochronology, trace elements and oxygen isotopes of zircon, microstructure and chemistry of plagioclase, and whole-rock elemental geochemistry and Sr-Nd isotopes to decipher the temporal compositional change and incremental growth of the Quxu granitoid batholith in the Gangdese magmatic belt, southern Tibet. The Quxu host granitoids are mainly metaluminous and calc-alkaline to high-K calc-alkaline in geochemistry, whilst the melanocratic microgranular enclaves (MMEs) and mafic dykes vary from calc-alkaline to shoshonitic series. New SIMS zircon U-Pb data suggest a prolonged history (ca. 16.6 Myr) for the Quxu batholith accompanied by several episodes of intermediate–mafic magma replenishments. Zircon $\delta^{18}O$ and whole-rock $(^{87}Sr/^{86}Sr)_i$ values fluctuate from ~5.6‰ to ~6.8‰ and from 0.7038 to 0.7085, respectively, while the whole-rock $\varepsilon_{Nd}(t)$ values show a fluctuated decrease from +5.2 to −4.5 with time. The calculated Ti-in-zircon temperature (574–903 °C) and oxygen fugacity (ΔFMQ −0.9 to ΔFMQ +3.2) of the granitoid magmas fluctuated as well. The youngest group of the host granitoids is distinguished by the most elevated Th/La (>1.5) and Th/Ce (>1.0) ratios and K_2O contents (>3.0 wt%) with evolved isotopic compositions, implying pronounced incorporation of supracrustal materials into the source region. Microstructural and compositional features of zircon and plagioclase from the host granitoids indicate that the incremental assembly of Quxu batholith was foremost facilitated by multiple episodes of magma recharge with distinct compositions and sources. The temporal variations of magma condition and composition throughout the lifetime of the magma reservoir highlight the importance of determining the longevity of batholiths and clarifying the discrepancy of individual magma pulses before deciphering the genesis of composite batholith. The aforementioned Sr–Nd–O isotopes show good correlations with the fluctuating whole-rock $(La/Yb)_N$ (2.7–68.5) and zircon Eu/Eu* (0.02–1.26) ratios, which further affirms episodic *syn*-collisional crustal thickening and episodic input of supracrustal material in magma sources. Based on the spatiotemporal variations of geochemistry, we propose a zoned incremental growth model to better illuminate the detailed processes of the incremental amalgamation of the Quxu batholith.

1. Introduction

Granites (sensu *lato*) are prominent constituents to assemble the continental crust and their widespread occurrence makes the Earth distinguished from other planets (e.g., Campbell and Taylor, 1983; Moyen et al., 2021). Thus, fingerprinting the detailed formation and evolution of granitic magma chambers/reservoirs can shed light on the understanding of crustal accretion and evolution. A growing number of studies have focused on the processes of magmatic reservoirs (e.g., Annen et al., 2006; Gaynor et al., 2023; Memeti et al., 2022; Zhang et al., 2021) and a pressing scientific issue is to constrain the lifetime and temporal evolution of large silicic magma reservoirs within the crust (e.g., Wang et al., 2021). This issue has become more elaborate in the last two decades, as inspired by the conjunction of high-precision zircon U-

* Corresponding author.
E-mail addresses: zyz_nju@smail.nju.edu.cn (Y.-Z. Zhang), wxl@nju.edu.cn (X.-L. Wang), huxm@nju.edu.cn (X.-M. Hu), ljy@nju.edu.cn (J.-Y. Li), dehong@nju.edu.cn (D.-H. Du), diwang@nju.edu.cn (D. Wang).

https://doi.org/10.1016/j.lithos.2023.107466
Received 28 November 2023; Received in revised form 14 December 2023; Accepted 14 December 2023
Available online 21 December 2023

Pb dating, in situ mineral micro-analysis, numerical simulation and geophysical observation (e.g., Annen et al., 2006; Gaynor et al., 2023; Memeti et al., 2022).

Incremental growth of huge batholiths has been proven to be very common in granite formation. Benefited from new precise zircon U-Pb geochronologic data, Coleman et al. (2004) demonstrated that the Tuolumne intrusive suites within Sierra Nevada cannot simply originate from a single magma chamber, but from incremental assembly of different pulses of granitic magma in a period of about 10 Myr (million years). Subsequent studies on archetypal batholiths (e.g., Gaynor et al., 2023; Karakas et al., 2017; Schaltegger et al., 2019; Wang et al., 2021) support the formation of large granite batholiths by incremental growth, rather than consolidating from a big magma tank (e.g., Glazner et al., 2004). Considering the pulsed incremental growth, a granite batholith always presents as a composite suite, and it is important to clarify the exact longevity, texture and component of each magmatic pulse prior to utilizing geochemical data to decipher the compositional variations and petrogenesis.

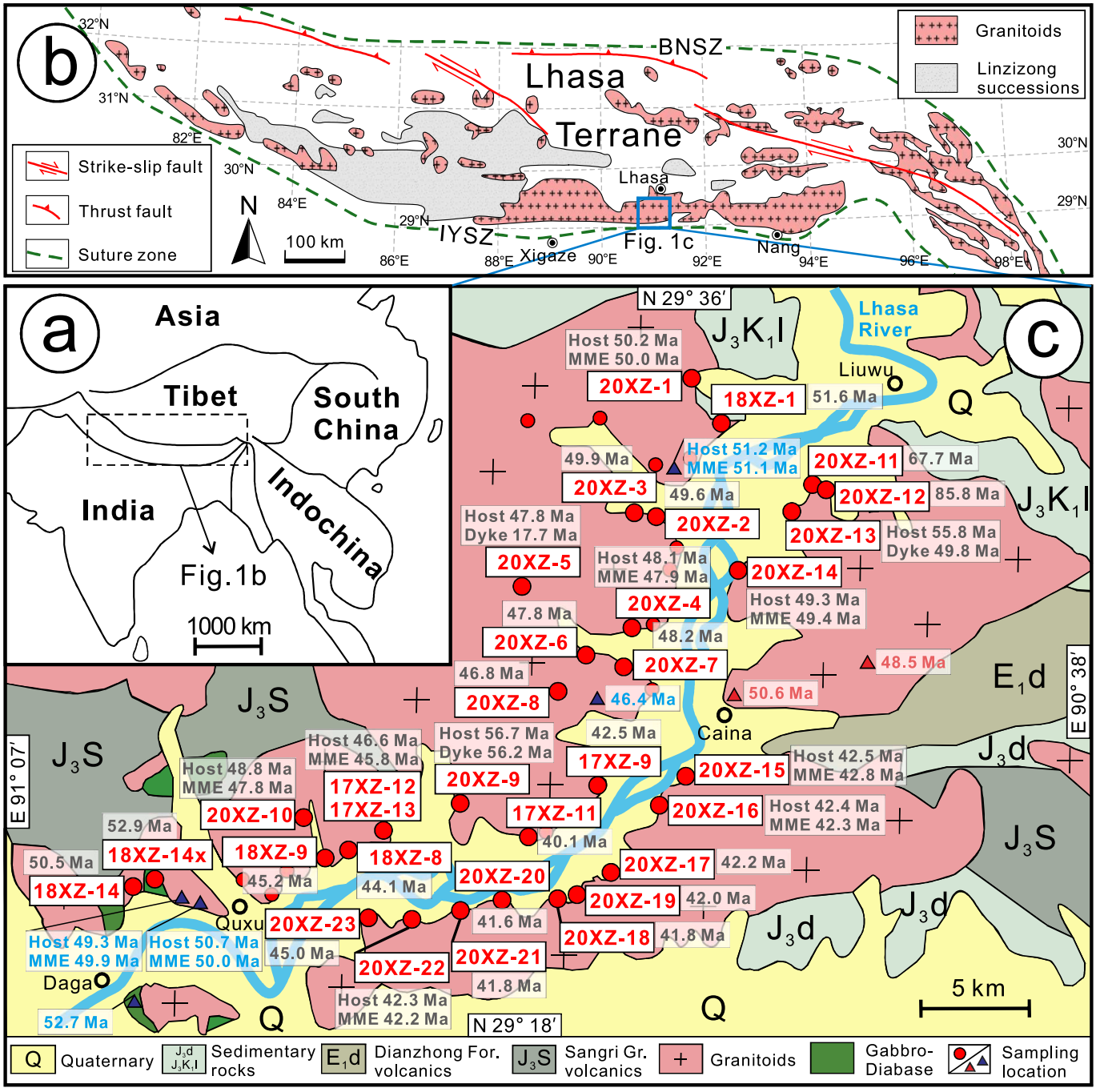

Fig. 1. Geological maps showing the location and geology of the Quxu batholith within the Gangdese magmatic belt. (a) Simplified map showing the Asian and Indian plates. (b) Regional geological map of the Lhasa terrane (modified after Ma et al., 2014). BNSZ = Bangong–Nujiang suture zone, IYSZ = Indus–Yarlung suture zone. (c) Geological map of the Quxu batholith showing the sampling locations (red circles) of this studies and previous studies (blue and red triangles, respectively). The blue triangles represent secondary ion mass spectroscopy date from Schärer et al. (1984) and Mo et al. (2005), while the red triangles represent LA–ICP–MS zircon U-Pb data from Ji et al. (2009) and Ma et al. (2017). (For interpretation of the references to colour in this figure legend, the reader is referred to the web version of this article.)

Serving as precious magmatic records responding to the subduction of Neo-Tethyan slab and Asia–India continental collision, the Gangdese magmatic belt (Late Triassic–Miocene) along the southernmost tip of Eurasia (Fig. 1a and b) provides a natural laboratory to investigate the structure of orogens, the formation mechanism of granite batholiths and the accretion and differentiation of the continental crust along convergent plate boundaries (Chung et al., 2009; Ji et al., 2009; Yin and Harrison, 2000; Zhu et al., 2023). Among the multifarious composite batholiths of distinct ages and rock types within the Gangdese magmatic belt, the Quxu batholith in the central Gangdese belt (Fig. 1c) has received great attention since 1980s. Previous studies on the batholith revealed a long lifetime (over 10 Myr) and attributed the batholith to extensive mixing between crust- and mantle-derived magmas during continental collision (e.g., Ji et al., 2009; Ma et al., 2017; Mo et al., 2005; Ruan et al., 2019; Schärer et al., 1984; Wang et al., 2019; Wen et al., 2008; Yu et al., 2023). It is an archetypal granite batholith, mainly composed of intermediate–felsic rocks with subordinate gabbros and dioritic dykes (Mo et al., 2005; Wen et al., 2008). Located at the frontier of the hanging wall in the continental collision zone, the Quxu batholith is well placed to chronicle considerable information on (1) the magmatic responses to collision, (2) the formation of magma reservoirs, (3) the transition of geodynamic regimes, (4) the crust-mantle interaction, and (5) the growth and reworking of continental crust. Hence, it is necessary to conduct a more systematic geochronology analysis integrated with geochemistry discussion on the Quxu batholith to explore the accretion history of silicic magma reservoir.

Here we present an integrated study involving detailed high-precision zircon SIMS U-Pb dating, trace element and oxygen isotope analyses combined with field and petrography observation, mineral chemistry, whole-rock major and trace element and Sr-Nd isotope data to probe into the incremental growth history and formation mechanism for the Quxu batholith. The new data allow us to identify an incrementally amalgamated magma reservoir corresponding to episodic magma recharge along with crustal thickening and reworking during the regional tectonic regime transition from subduction to continent–continent collision.

2. Geological background and sampling

The Tibetan Plateau is commonly classified from south to north into the Himalayan orogen, and Lhasa, Qiangtang, Songpan–Ganzi, Kunlun–Qilian terranes, separated by the Indus–Yarlung, Bangong–Nujiang, Jinshajiang and Animaqen suture zones, respectively (e.g., Ji et al., 2009; Yin and Harrison, 2000; Zhu et al., 2022). The Gangdese magmatic belt is distributed along the southernmost part of the Lhasa Terrane and is separated from the Himalayas to the south by the Indus–Yarlung suture zone (Fig. 1b). It extends ca. 1600 km in length and over 100 km in width and mainly consists of intermediate–felsic igneous rocks with subordinate mafic rocks due to the Mesozoic northward subduction of Neo-Tethyan oceanic slab and Cenozoic continent–continent collision between Asian and Indian plates (e.g., Chung et al., 2009; Ji et al., 2009; Yin and Harrison, 2000; Zhu et al., 2023). The intrusive rocks of the Gangdese magmatic belt were mainly emplaced between Middle Triassic to Miocene (ca. 245–10 Ma), and four main active episodes of granitic magmatism were distinguished in the Gangdese area based on available geochronologic data (e.g., Ji et al., 2009; Zhu et al., 2022, 2023): Late Triassic–Jurassic (205–152 Ma), Cretaceous (109–80 Ma), Palaeocene–Eocene (65–41 Ma), and Oligocene–Miocene (33–13 Ma). Among them, the Palaeocene–Eocene period has been interpreted to record the tectonic transition from slab subduction to continent collision (Yin and Harrison, 2000; Zhu et al., 2022, 2023).

The Quxu batholith in the central Gangdese belt, adjacent to the Quxu County, and south of Lhasa City, is cut by the Lhasa River into eastern and western parts (Fig. 1c). The batholith has a length of ca. 50 km and a width of ca. 30 km (Fig. 1c) and contains predominant intermediate–felsic rocks with less gabbros and mafic dykes. It was intruded into Late Jurassic–Early Cretaceous Linbuzong Formation sedimentary rocks and Late Jurassic Duodigou Formation sedimentary rocks and Sangri Group volcanics, accompanied with simultaneous Eocene Dianzhong Formation volcanics (Ma et al., 2017). The Quxu batholith is characterized by the extensive occurrences of various melanocratic microgranular enclaves (MMEs) (Fig. 2), which were previously recognized as evidence of magma mixing (Mo et al., 2005; Wang et al., 2019). There has been some dating work by LA-ICP-MS (laser ablation–inductively coupled plasma–mass spectrometry) and SIMS on zircon grains from the granitoids, and the results suggest the batholith was emplaced during Eocene (ca. 55–45 Ma) (Ji et al., 2009; Ma et al., 2017; Mo et al., 2005; Schärer et al., 1984; Wang et al., 2019; Wen et al., 2008), roughly coeval with or soon after the collision (Parsons et al., 2020; Zhu et al., 2023). However, the dating results are overlapping and spatio-temporally irregular, which requires more comprehensive sampling and geochronology analyses. In this study, we collected 38 fresh rock samples, including 27 host granitoid samples, 8 MME samples and 3 mafic dyke samples along the road-cut profiles from both parts of the Quxu batholith (Fig. 1c).

3. Analytical methods

Detailed analytical methods are presented in the Appendix A.

4. Results

4.1. Petrography

The Quxu batholith shows typical plutonic features inferred from the massive structure (Fig. 2) and medium- to coarse-grained holocrystalline textures of the granitoid samples (Fig. 3). Detailed sample descriptions on the sampling location, rock type, mineral assemblage as well as U-Pb age are combined together and listed in the Supplementary Table S1.

The medium- to coarse-grained host granitoids in the Quxu batholith vary in rock type from diorite to granite (Fig. 3a–f; Table S1). These lithofacies change gradually without distinct contact boundaries observed in the field. The host granitoids mainly consist of plagioclase, alkali feldspar, hornblende, biotite and quartz, associated with accessory minerals of titanite, zircon, apatite, Fe-Ti oxides, monazite, epidote and allanite (Fig. 3a–f; Table S1).

The fine-grained MMEs mainly show apparent magmatic textures and have gabbroic and dioritic compositions with rare norite and monzonite (Fig. 3g–j). The MMEs are mainly composed of plagioclase, hornblende and biotite, associated with accessory minerals of titanite, zircon, apatite, Fe-Ti oxides, monazite and epidote (Fig. 3g–j; Table S1).

The fine- to medium-grained mafic dykes are gabbro and diorite (Fig. 3k and l). The mafic dykes mainly contain plagioclase, hornblende, biotite, Fe-Ti oxides and clinopyroxene, associated with accessory minerals of titanite, zircon, apatite, monazite and epidote (Fig. 3k and l; Table S1).

4.2. Plagioclase compositional mapping and chemistry

Representative plagioclase grains with zoning textures were selected for major and trace element analyses and compositional mapping. The data are presented in the Supplementary Table S2. The compositional maps (Fig. 4a–c) show conspicuously intra-grain fluctuating Ca contents of plagioclase in the host granitoids (20XZ-2-1, 20XZ-17-1 and 20XZ-5-4). The resorption zones, spike zones and wavelike calcic belts (or calcic “spikes”; cf. Baxter and Feely, 2002) are recognized based on optical microscopic observation, BSE image and compositional mapping (Figs. 3, 4 and Fig. S1 in the Appendix A). Notably, the resorption zones are generally accompanied with poikilitic Ca-rich (e.g., An-rich feldspar, hornblende and apatite) and Fe-rich (e.g., Fe-Ti oxides and biotite) minerals, and occasionally with sieve structures (Fig. 4a–c).

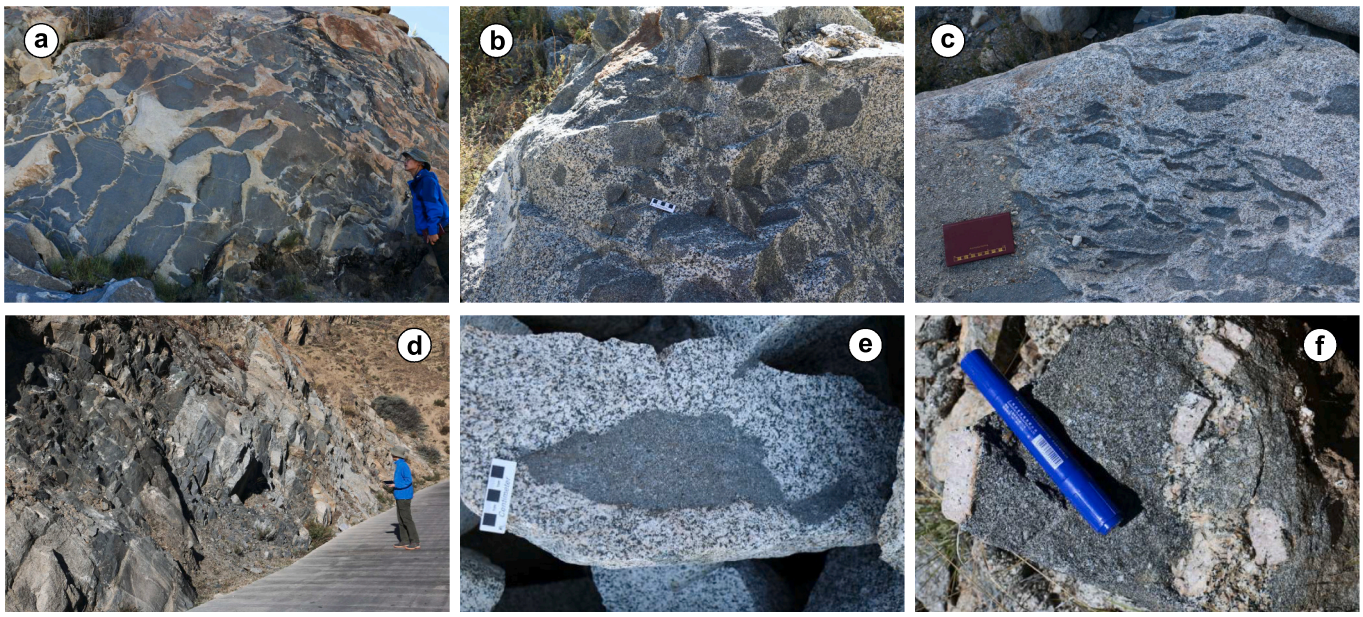

Fig. 2. Field photographs showing the MMEs and mafic dykes in the Quxu batholith. (a) The large MME swarm showing sharp contacts with the host granitoids. (b) The MME swarm containing different enclave shapes. (c) The elongated MMEs within the host granitoids. (d) The mafic dykes intruding into the host granitoids with sharp contacts. (e) The deformed MMEs showing twisted contacts with the host granitoids. (f) The K-feldspar phenocrysts incorporated into the MMEs and the presence of back veining of the host granitoids.

The growth of plagioclase in host granitoids generally started from a relatively sodic core ($Ab_{55–67}An_{32–44}Or_{1–2}$) with a remarkable calcic mantle (spike zone; $Ab_{46–62}An_{36–53}Or_{1–2}$), followed by alternating growth of several Na-rich and Ca-rich compositional belts. The calcic belts give rise to the An-rich spikes in the An content diagrams (Fig. 4 a–c). The outermost edges of plagioclase grains are generally surrounded by more sodic rims ($Ab_{66–82}An_{17–33}Or_{1–2}$) than cores. The concentrations of Fe (250–9700 ppm), Mg (7.31–2710 ppm), Mn (2–972 ppm) and Ti (4.76–190 ppm) of these plagioclase grains manifest large variations. No obvious correlation of Sr (750–1570 ppm), Ba (37–1150 ppm) and La (0.08–13.0 ppm) abundances with An contents was observed. Notably, the Fe, Mg, Ti and Mn concentrations located within or adjacent to the resorption and spike zones and calcic belts are conspicuously elevated and form "spikes" in compositional profiles (Fig. 4 a–c).

The plagioclase in mafic rocks (e.g., 18XZ-14x-2; Fig. 4d) has Ca-rich cores ($Ab_{12–15}An_{85–88}Or_{0}$), abruptly or gradationally surrounded by Na-rich rims ($Ab_{55–63}An_{35–44}Or_{1–2}$), showing typical normal zoning of plagioclase. The Fe (1020–2780 ppm), Mg (26–715 ppm), Ti (59–300 ppm) and Mn (17.3–67.4 ppm) concentrations of plagioclase show limited variations compared with those from the host granitoids. Especially, the abundances of Sr (970–1130 ppm), Ba (64–200 ppm) and La (0.87–9.22 ppm) decrease from the An-rich cores to the An-poor rims, exhibiting roughly negative correlations with the An contents (Fig. 4d).

4.3. Zircon CL image, U-Pb age and oxygen isotopes

The long prismatic to granular zircon grains are transparent, colorless to yellowish. The lengths of zircon crystals vary from 60–300 μm to 50–200 μm for the host granitoids and mafic components (MMEs and mafic dykes) (Fig. 5a), respectively. Most of them present archetypal oscillatory zoning, suggesting an igneous origin (Fig. 5a). Inherited grains/cores were discovered and further determined by SIMS U-Pb dating (Fig. 5a). Four zircon types were classified based on the CL structure, morphology and U-Pb dating results (cf. Miller et al., 2007; Fig. 5a). Type I zircon is autocryst without core–rim texture (i.e., inherited core with newly crystallized rim) or pronounced intra-grain U-Pb age difference (Fig. 5a). Type II zircon contains antecryst core showing marginally older age than their newly grown rims (Fig. 5a). Type IIA (dark core + bright rim) and Type IIB (normal core + bright rim) zircons are sub-divided on the basis of the appearance of cores and CL intensity (Fig. 5a). The edges of the Type II zircon core frequently display partial dissolution features (Fig. 5a). Type III zircon is fabricated of xenocryst core and newly grown rim, indicated by the sufficiently older ages of core (Fig. 5a). Type IV zircon is characterized by its normally grown core with narrow dark rim (Fig. 5a) without apparent core–rim age differences.

The data of zircon U-Pb isotopic dating are listed in Supplementary Table S3, while the U-Pb concordia diagrams are presented in the Supplementary Fig. S2 in the Appendix A. U-Pb dating analyses on xenocrystic grains/cores of Type III zircon yield $^{206}Pb/^{238}U$ (≤1000 Ma) and $^{207}Pb/^{206}Pb$ (>1000 Ma) ages of 68.7–1763 Ma. The remaining analyses on zircon rims yield weighted mean $^{206}Pb/^{238}U$ ages from 56.7 ± 0.6 Ma to 40.1 ± 0.5 Ma for the host granitoids and associated MMEs, and from 56.2 ± 0.7 Ma to 46.6 ± 0.5 Ma for the mafic dykes (Fig. S2). All of the weighted mean ages of the host granitoids and MMEs are consistent within uncertainties, which we interpret to suggest a co-magmatic origin of the two components. Three magmatic peaks ($p1$ = 57–55 Ma, $p2$ = 51–46 Ma and $p3$ = 43–40 Ma) and two lulls ($l1$ = 55–51 Ma and $l2$ = 46–43 Ma) are identified based on the kernel density estimates for the zircons and rocks of the Quxu batholith (Fig. 5b and c). The data of zircon oxygen isotopes are presented in Supplementary Table S4. The zircon $\delta^{18}O$ of the host granitoids shows the widest range (5.6‰–6.8‰), while those of the MMEs and mafic dykes are similar (5.9‰–6.3‰ and 5.8‰, respectively). The host diorite, quartz diorite and granite rocks share similar zircon $\delta^{18}O$ (5.6‰–6.1‰), while the zircon $\delta^{18}O$ of the host granodiorite (5.8‰–6.8‰) and quartz monzonite (6.0‰–6.7‰) show wider variations. These values are within or slightly higher than the range of mantle zircon (5.3‰ ± 0.6‰, 2σ; Valley, 2003).

4.4. Zircon trace elements

The data of zircon trace elements are listed in Supplementary Table S5. Ti concentrations of magmatic zircon grains from the host granitoids vary from 0.8 to 30 ppm, whilst those of the MMEs and mafic dykes range from 0.8 to 25 ppm, yielding Ti-in-zircon geothermometer

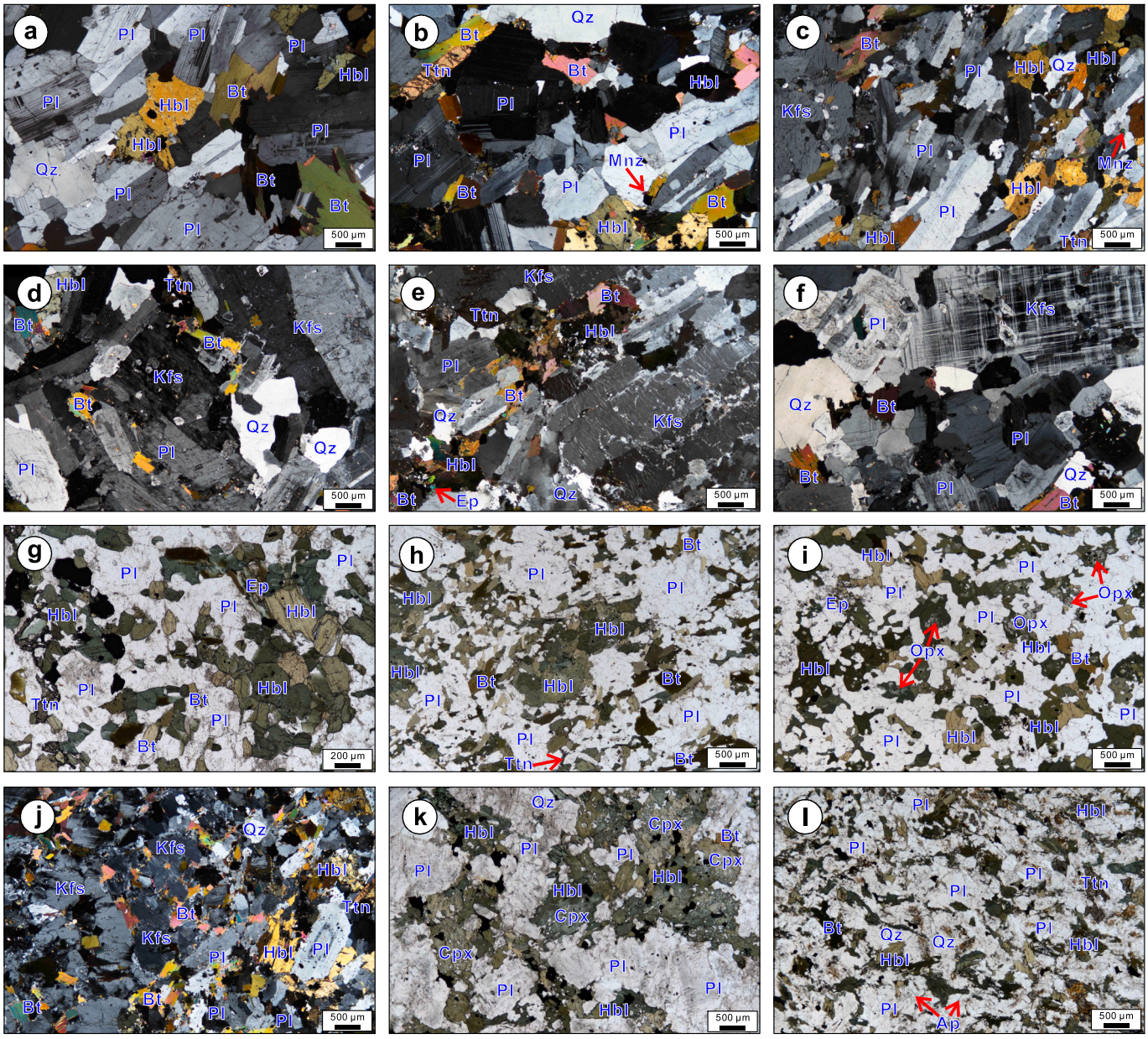

Fig. 3. Photomicrographs of the representative rock types in the Quxu batholith showing the main mineral assemblages. (a) Diorite (cross-polarized light). (b) Quartz diorite (cross-polarized light). The resorption zones in plagioclase can be observed in some grains. (c) Granodiorite (cross-polarized light). The resorption zones in plagioclase can be observed in some grains. (d) Quartz monzonite (cross-polarized light). The compositional zoning in plagioclase can be observed in some grains. (e) Syenogranite (cross-polarized light). (f) Granite (cross-polarized light). The resorption zones in plagioclase can be observed in some grains. (g) Gabbroic MME (plane-polarized light). (h) Dioritic MME (plane-polarized light). (i) Noritic MME (plane-polarized light). The resorption zones in plagioclase can be observed in some grains. (j) Monzonitic MME (cross-polarized light). (k) Gabbro (plane-polarized light). (l) Diorite (plane-polarized light).

($T_{Ti\text{-}Zrn}$; Ferry and Watson, 2007) results for the host granitoids and mafic components of 576–903 °C and 544–824 °C, respectively (Fig. 6a). Given the ubiquitous titanite presence in the host granitoids and mafic rocks, the activity of TiO_2 was set to 0.7 (Ferry and Watson, 2007) for these rocks. The activities of SiO_2 were set to 1.0 and 0.6 for the felsic and mafic rocks, respectively. It is noteworthy that the majority of $T_{Ti\text{-}Zrn}$ results of the host granitoids and mafic rocks roughly straddle between 600 °C to 800 °C with few outliers (Fig. 6a). The concentrations of Ce, U and Ti of zircon are used for calculating the magma oxygen fugacity (f_{O_2}; Fig. 6b) following the method of Loucks et al. (2020). The f_{O_2} values of the host granitoids and mafic rocks vary from ΔFMQ (refer to fayalite-magnetite-quartz buffer) – 0.9 to ΔFMQ +3.2, and from ΔFMQ – 0.8 to ΔFMQ +2.3, respectively.

The analysed zircon grains commonly show fractionated rare earth element (REE) patterns with $(La/Yb)_N < 0.001$, positive Ce anomalies with chondrite-normalized $Ce/(La \times Pr)^{0.5}$ ratios (Ce/Ce*) higher than 21 and negative Eu anomalies with chondrite-normalized $Eu/(Sm \times Gd)^{0.5}$ ratios (Eu/Eu*) mostly lower than 0.8, which together demonstrate igneous origins for the zircon grains following the criteria of Hoskin and Schaltegger (2003). Zircon grains from the host granitoids generally have higher total REE concentrations (ΣREE >70 ppm), U/Yb (0.3–25 ppm) and Ce/Ce*, and lower Zr/Hf (24–62; Fig. 6c) than those of the mafic components. Most of the analysed zircon grains have similar Th/U (>0.1 and up to 2.6; Fig. 6d).

4.5. Whole-rock elements and Sr-Nd isotopes

The data of whole-rock major and trace elements are presented in

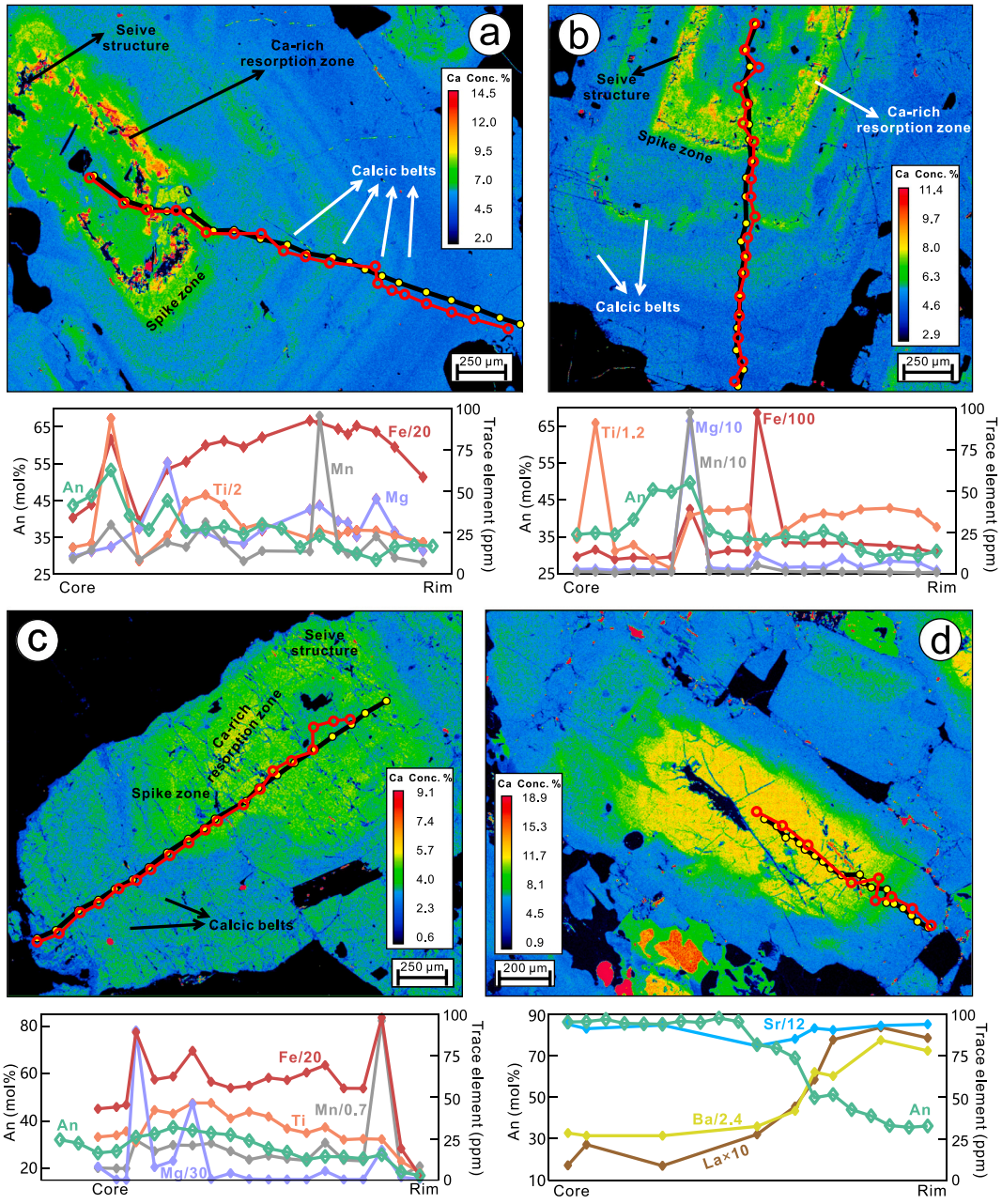

Fig. 4. Compositional mapping images and profiles showing the zoning patterns, and contents of An (anorthite) and trace elements of the host granitoids (a–c) and MME (d). (a) 18XZ-1-3. (b) 20XZ-17. (c) 18XZ-9-1. (d) 18XZ-1-1.

Supplementary Table S6. The host granitoids have various SiO_2 and K_2O contents of 55.2 wt%–73.5 wt% and 1.17 wt%–4.74 wt%, respectively, and they generally show calc-alkaline to high-K calc-alkaline geochemical characteristics (Fig. S3a in the Appendix A). Compared with the mafic dykes and MMEs, the host granitoids have lower contents of MgO (0.41 wt%–3.18 wt%), $Fe_2O_3^T$ (1.28 wt%–7.67 wt%), MnO (0.01 wt%–0.19 wt%) and CaO (1.25 wt%–7.93 wt%) and higher SiO_2 contents. Most of the rocks from the Quxu batholith exhibit metaluminous feature with aluminum saturation index [ASI; molar $Al_2O_3/(CaO + Na_2O + K_2O)$] lower than 1.0, except one granite sample (18XZ-14-1). The host granitoids fall in the fields of monzo-diorite, monzonite, quartz monzonite, diorite, granodiorite and granite according to rock classification diagram, whereas the mafic rocks belong to gabbro, monzogabbro, monzo-diorite, diorite and monzonite (Fig. S3b in the Appendix A).

Overall, the rocks from the Quxu batholith are characterized by their variable degrees of enrichments in large-ion lithophile elements (LILEs; e.g., Rb) and Th, U, Pb, and depletions in high-field-strength elements (HFSEs; e.g., Nb, Ti, P). The host granitoids tend to have relatively higher concentrations of highly incompatible elements (HIE; e.g., Th, Rb, Pb) and Sr/Y (5.8–67) and Rb/Sr (0.03–1.40) ratios than the synchronous mafic rocks (Fig. S3c; Table S6 in the Appendix A).

The felsic and mafic rocks both display fractionated REE patterns which are enriched in light REEs and depleted in heavy REEs with slightly negative or negligible Eu anomalies (0.5–1.0 and 0.6–1.0, respectively). Meanwhile, the host granitoids generally have higher $(La/Yb)_N$ (2.7–68.5) than the coeval mafic rocks. Nevertheless, the MMEs have the highest ΣREE (154–433 ppm) than the host granitoids and mafic dykes (Fig. S3d; Table S6 in the Appendix A).

The data of whole-rock Sr-Nd isotopes are presented in supplementary file Table S7. The host granitoids have variable initial $^{87}Sr/^{86}Sr$ [$(^{87}Sr/^{86}Sr)_i = 0.7038–0.7085$; Fig.3e] ratios and $\varepsilon_{Nd}(t)$ values (−2.4 to

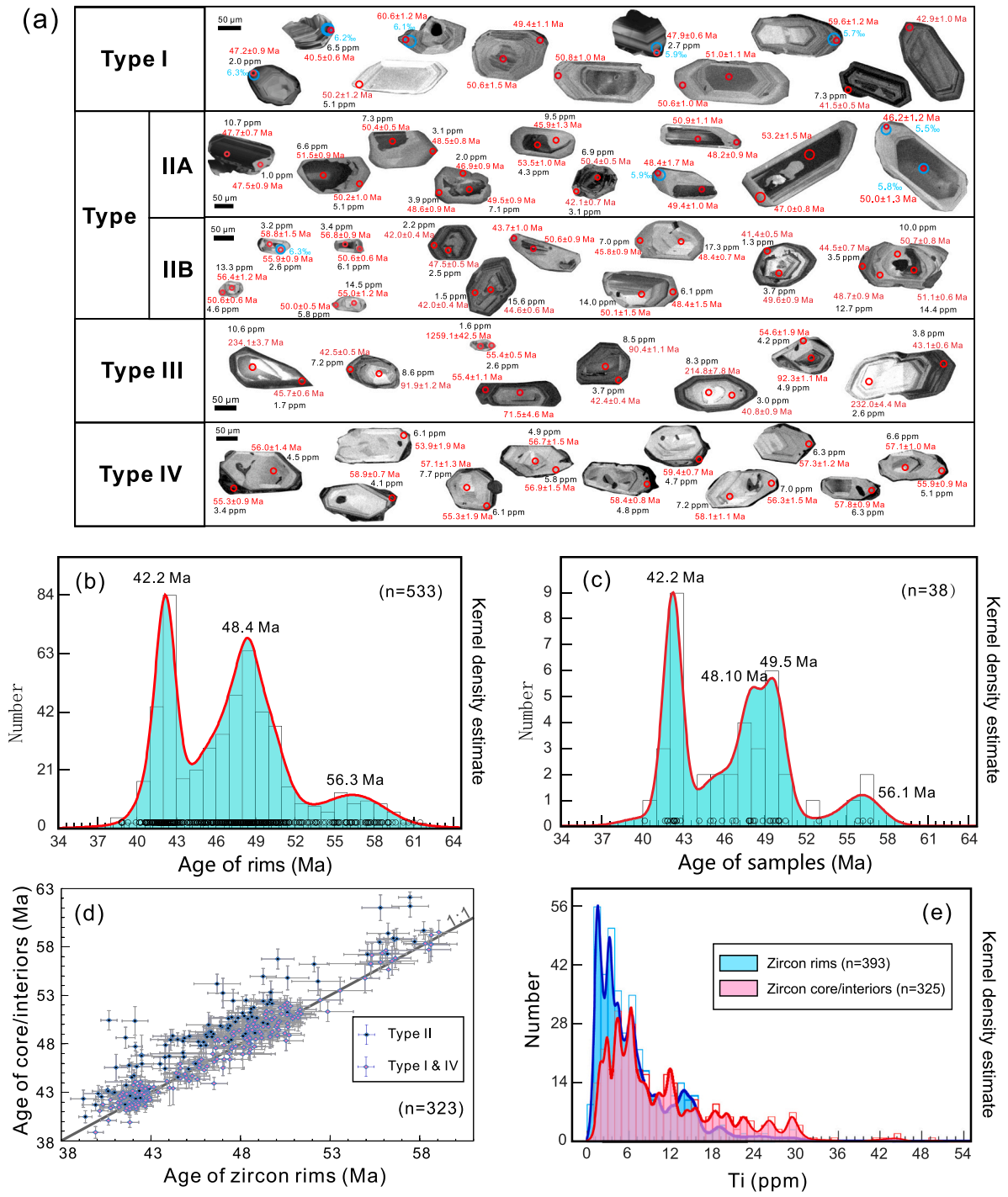

Fig. 5. Diagrams showing the features of zircon types and SIMS zircon U-Pb dating and Ti concentration results of the Quxu batholith. (a) CL signatures of representative zircon types. (b) Kernel density estimates for the zircon U-Pb dating results of zircon rims. (c) Kernel density estimates for the zircon U-Pb dating results of rock samples. (d) Plot of comparison for the U-Pb dating results of the zircon core/interiors and rims (except Type III zircons). (e) Kernel density estimate for the Ti concentrations in zircon core/interiors and rims. The red, black and light blue letters in (a) represent zircon U-Pb age, Ti concentration and $\delta^{18}O$, respectively. (For interpretation of the references to colour in this figure legend, the reader is referred to the web version of this article.)

+5.2; Fig.3f). The MMEs and mafic dykes, in particular the latter, have more depleted Sr-Nd isotopic compositions than the host granitoids with $(^{87}Sr/^{86}Sr)_i$ of 0.7045 to 0.7075 and $\varepsilon_{Nd}(t)$ of −4.5 to +3.7, and $(^{87}Sr/^{86}Sr)_i$ of 0.7038 to 0.7049 and $\varepsilon_{Nd}(t)$ of −4.1 to +4.6, respectively (Fig. S3e and f; Table S7 in the Appendix A).

5. Discussion

5.1. Temporal and spatial patterns of the incremental growth of the Quxu granite batholith

It is widely acknowledged that a large batholith commonly experiences a protracted history (over Myr range) with several episodes of magma replenishment and subsequent hybridization which could give

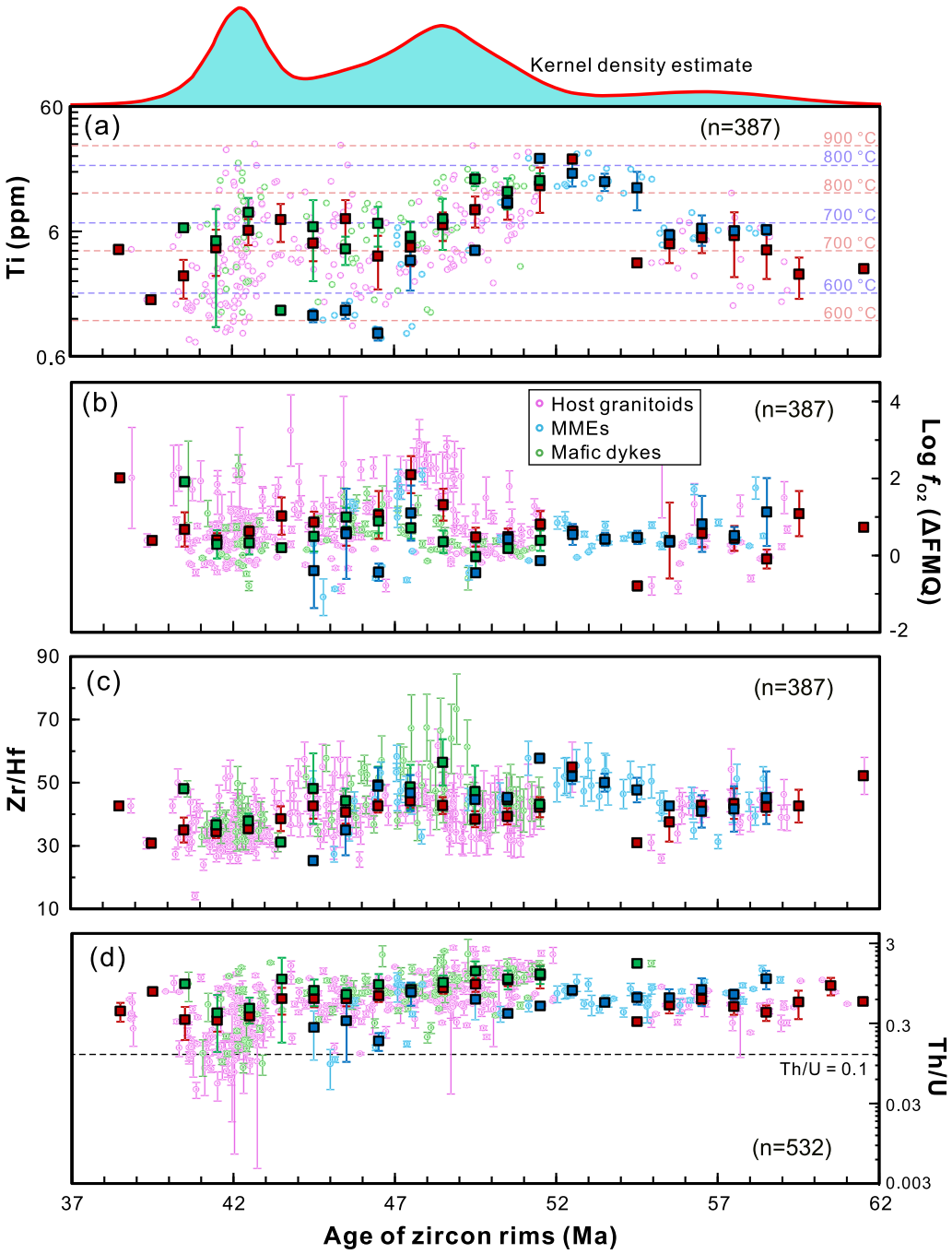

Fig. 6. Compositional changes of 1 Ma-binned average (2SE) of selected zircon compositions and calculated O_2 fugacity. (a) Zircon Ti concentrations. The orange dashed lines represent calculated values for the host granitoids, while the purple ones are for the mafic rocks. (b) Oxygen fugacity calculated from zircon U, Ti and Ce abundances. (c) Zircon Zr/Hf. (d) Zircon Th/U. (For interpretation of the references to colour in this figure legend, the reader is referred to the web version of this article.)

rise to temporal-compositional fluctuations in melts and incremental growth of magma reservoirs (e.g., Claiborne et al., 2006, 2010; Memeti et al., 2022; Miller et al., 2007; Schaltegger et al., 2019). Determining the lifetime of large composite batholith is fundamental to the subsequent petrographic and tectonic interpretations based on the geochemical heterogeneity and spatial-temporal variations of magma compositions.

Although some zircon U-Pb dating studies have been published for the Quxu batholith (e.g., Ji et al., 2009; Ma et al., 2017; Mo et al., 2005; Schärer et al., 1984; Wang et al., 2019; Wen et al., 2008), the comprehensive geochronology analysis remains limited. In particular, different dating results were obtained for the same rock types in the same sampling locations, which increase the ambiguity of the previous age results and prevent further detailed geochemical discussion on the formation of the batholith. The characteristics of CL images (oscillatory and sector zoning) and trace element compositions (positive Ce anomaly, negative Eu anomaly and enrichment of HREE over LREE) together suggest the igneous origin for the analysed zircon grains of this study. Hence, the newly acquired SIMS zircon U-Pb geochronologic data from this study allow us to unravel a complex amalgamation history of the long-lived silicic magma reservoir for the Quxu batholith.

Considering the presence of apparent core–rim structure in some

zircon grains, we take the analyses on zircon rim to calculate the crystallization ages for all the rocks. As shown in Fig. 5b and c, the new dating results on zircon rims vary smoothly from ~61 Ma to ~38 Ma, while the weighted average mean ages of rock samples range from 56.7 Ma to 40.1 Ma. Three main magmatism peaks (~56 Ma, ~48 Ma and ~42 Ma) are identified from the Kernel density estimates for zircon crystallization ages. It is noted that the new dating results of this work reveal a long residence time (ca. 16.6 Myr) for the whole Quxu silicic magma reservoirs. Since the time required to consolidate a single batch of magma is generally less than hundreds of kiloyears according to high-precision CA-ID-TIMS and compositional and thermal diffusion methods (Coleman et al., 2004; Jiang et al., 2023; Wang et al., 2021), the incremental formation of the batholith requires prolonged external magma recharges to maintain the mushy zone and avert complete solidification (e.g., Karakas et al., 2017), which is in accordance with the systematic differences of rock type varying with U-Pb age.

It is noteworthy that the petrographic characters change with time in the Quxu batholith. According to the new systematic SIMS zircon U-Pb dating results of this study, for the host granitoids, the ~56 Ma granitoids include granite and granodiorite and they have similar mineral assemblages with different percentages (Table S1 in the Appendix A). The 51–49 Ma rocks occupy the largest area of the batholith and vary in the greatest extent from diorite, quartz diorite, quartz monzonite, granodiorite to granite (Table S1). The following 48–47 Ma rock samples manifest a limited range from quartz diorite to quartz monzonite, the 45–44 Ma rocks are granodiorite with similar mineral assemblages, while the 42–40 Ma rocks are mostly quartz monzonite with minor granodiorite, granite and syenogranite (Table S1). For the MMEs, the ~50 Ma samples are gabbro with the presence of clinopyroxene and less orthopyroxene, the 48–47 Ma samples are gabbroic to dioritic without pyroxene, while the ~42 Ma samples range from diorite to monzonite (Table S1). The mafic dykes are rare and mainly occur as gabbros and diorites (Fig. 2d). In summary, the new SIMS zircon U-Pb geochronologic data of this study suggest a considerably long-lived (ca. 16.6 Myr) magma reservoir with episodic magma reactivation events. The multiple emplacements of silicic magma and recharges of mafic magma both contributed to the incremental growth of the Quxu batholith. Detailed evaluations on the formation and evolution processes of the magma reservoir will be discussed in the following sections.

5.2. *Episodic magma recharge and hybridization events recorded by zircon and plagioclase*

Considering the pervasive occurrences of MMEs (Fig. 2) with identical crystallization ages with their host granitoids, we reckon that the multiple recharges of mafic magma released sufficient heat (and volatiles) to rejuvenate the silicic magma reservoir and contributed greatly to the incremental growth of the Quxu batholith through hybridization. Notably, the repeated replenishments identified by the core–rim discrepancies in zircon and the zoning patterns in plagioclase (Figs. 5a and 4a–c) from the host granitoids are assumed to chronicle detailed episodic mafic magma recharges and hybridizations.

The U-Pb dates and structure discrepancies between the Type II zircon rims and cores unveil a fluctuating growth of magma reservoir. As summarized in Fig. 5d, the dates of zircon cores/interiors and rims are identical within uncertainties for the Types I and IV zircons. However, as for the Type II zircon domains, they present slightly older dates (still within the majority of the zircon) of cores compared with rims, especially for the ~56 Ma, 50–47 Ma, ~44 Ma and ~42 Ma zircon groups. Furthermore, the old dates of these cores perfectly correspond to the earlier periods of magmatism within this region, which indicates the recycling and subsequent regrowth of antecrysts ascribed to the injection of new magma pulse(s) during incremental growth as suggested by previous studies (e.g., Miller et al., 2007). This episodic injection (or magma recharge) is further supported by CL signatures that the partially dissolved cores are surrounded by new rim growths in those zircons (Fig. 5a). Some Type II zircons exhibit clear core–rim structures but without intra-grain dating differences. This may reflect the rapid replenishment of antecrysts due to the new batches of magma intruded immediately after their crystallization, which is exceeding the analytical limits of SIMS.

The $T_{Ti\text{-}Zrn}$ results of zircon core/interior and rim domains show conspicuous variations as well. On the one hand, the Ti concentrations (Table S5 in the Appendix A) of zircon core/interior domains are broadly higher than those in rim domains, reflecting a prolonged cooling process for the magma reservoir (Fig. 5e). On the other hand, the $T_{Ti\text{-}Zrn}$ results of the host granitoids, MMEs and mafic dykes exhibit temporal changes with several rises and falls (Fig. 6a), which are potentially caused by periodic magma reactivation and subsequent cooling. It's worth noting that zircon rims failed to record the heating events (i.e., high Ti concentrations) caused by the multiple magma recharges. One possible explanation is the delayed regrowth of the new zircon rims. The mafic–intermediate magmas are thought to be zircon undersaturated owing to high temperatures and inadequate Zr concentrations (Watson and Harrison, 1983; Miller et al., 2007). After rapid magma replenishment, the released heat and the modified melt composition gave rise to the incomplete dissolution of zircon antecryst within the crystal mush (e.g., Bindeman and Melnik, 2016). Zircon rims were unable to crystallize due to the high thermal and zircon-undersaturation states of the mixed melts. Only when magma conditions were approaching lower temperatures and Zr-saturation, could zircon rims start to grow along the edge of partially resorbed zircon antecrysts. Hence, the newly grown zircon rims commonly failed to record the high-temperature stage of the heating event.

The microstructural signatures and compositional zoning patterns of plagioclase are believed to chronicle the evolution of differing melt compositions and physical properties and multifarious magmatic processes (e.g., Baxter and Feely, 2002; Blundy and Wood, 1991; Browne et al., 2006; Ma et al., 2017; Pietranik and Koepke, 2014), due to the sluggish CaAl–NaSi interdiffusion rates within the crystal structure (Grove et al., 1984). Many factors have been proposed for the complicated zoning patterns and variations of An contents in plagioclase mainly including temperature, pressure, water content and melt composition (e.g., Castro, 2001; Coote and Shane, 2016; Pietranik and Koepke, 2014; Singer et al., 1993).

The increase of temperature and decrease of pressure will change the An contents of crystallized plagioclase. However, the change of temperature in closed-systems could only give rise to ~5–10 mol% An fluctuations in plagioclase (e.g., Singer et al., 1993), while changing the pressure generally has slighter influence on the composition of plagioclase (<10 mol% An; Castro, 2001; Pietranik and Koepke, 2014). The An contents in plagioclase grains from the Quxu granitoids present large turbulences up to 24 mol%, which cannot be solely attributed to the change of temperature or pressure. Instead, Singer et al. (1993) demonstrates that mixing of mafic and silicic melts is a viable mechanism for producing compositional shifts of >10 mol% An content in plagioclase.

The enhancement of water content (or H_2O partial pressure) in melts is prone to raise the An contents of the newly crystallized plagioclase (Coote and Shane, 2016). Nonetheless, the widespread hornblende grains in the Quxu host granitoids with different ages imply limited fluctuations of water contents (Scaillet and Evans, 1999). Moreover, the rises of water content of melts would reduce the solidus and liquidus, and further lead to pervasive resorption textures in various minerals, which, however, is not observed in our samples.

The Quxu composite batholith exhibits archetypal plutonic structures (Figs. 2 and 3) and is distinct from the volatile-rich volcanics. Thereby, the required drastic change of pressure or water contents seems impractical to account for the large variations of An contents and microstructural observations (resorption and spike zones and calcic belts) of this study. Most importantly, the fluctuations of temperature, pressure and water content exert little impact on the trace element concentrations (e.g., Fe, Ti, Mg, Sr, Ba, REEs) of plagioclase (e.g., Coote

and Shane, 2016), whereas the melt compositions and plagioclase/melt Nernst partition coefficients ($D^{Pl/Melt}$) of trace element are the major factors (Castro, 2001). Most $D^{Pl/Melt}$ values of trace elements predominantly depend on the An contents and manifest negative correlations during equilibrium crystallization, especially for Sr, Ba and REEs (e.g., Blundy and Wood, 1991). However, there is no correlation of Ba, Sr and REEs with An contents in the plagioclase grains from the host granitoids. Instead, the simultaneous rises of Fe, Mg, Ti and Mn concentrations and An contents in resorption zone and calcic belts (Fig. 4a–c) hint at the abrupt compositional turbulences induced by mixing with mafic magmas, which is also supported by previous studies (e.g., Coote and Shane, 2016; Ma et al., 2017).

The microstructural and compositional zoning patterns in plagioclase are therefore ascribed to the thermal and chemical turbulences induced by magma mixing, a commonly invoked process in the evolution of silicic systems in the upper crust (e.g., Baxter and Feely, 2002; Browne et al., 2006; Ma et al., 2017; Pietranik and Koepke, 2014). Inspired by the experiments of Castro (2001), we summarized the process of multiple magma recharges and hybridizations recorded by plagioclase of the Quxu host granitoids as follows:

(1) heat diffuses faster than chemistry, thus the intruding mafic magmas first released sufficient heat and increased the temperature of the host magmas and partially dissolved the adjacent pre-crystallized plagioclase grains;
(2) subsequent chemical hybridization with Ca-rich mafic magmas generated a non-equilibrium melt which was below its liquidus and Ca-oversaturated, and more mafic than the previous host magma (Castro, 2001). The compositionally undercooling hybridized melt would quickly crystallize An-rich plagioclase (Browne et al., 2006; Castro, 2001) along the resorption planes of the plagioclase grains, which remarked the generation of spike zones;
(3) meanwhile, the hot mixed melt would also give rise to the sieve textures in plagioclase, where the sieves were later filled with An-rich plagioclase (Browne et al., 2006);
(4) with hybridization proceeding, the host magmas and intruding magmas would establish re-equilibrium of temperature and composition (Castro, 2001), and lower An (sodic) plagioclase could crystallize surrounding the resorption and spike zones (Fig. 4a–c).

The subsequent pulse of mafic magma without abundant heat to partially dissolve the plagioclase grains would contribute to the overgrowth of An-rich plagioclase on previous grains once again, which denoted the formation of calcic belts (Fig. 4a–c). Consequently, the amount of resorption zones and calcic belts in plagioclase grain remarks the frequency of magma recharge and hybridization.

5.3. Compositional change along with incremental growth

Whole-rock geochemical analysis has been regarded as a powerful tool to elucidate the formation and evolution paces of magma reservoirs in terms of source heterogeneity, partial melting condition, crystal fractionation, magma mixing, and wall-rock contamination in the granite study of the last decade (e.g., Moyen et al., 2021; Moyen and Laurent, 2018; Yu et al., 2023; Zhang et al., 2021). Nevertheless, it should be noted that only in conjunction with the entire geological process could geochemistry data be properly utilized. Otherwise, it will result in flawed interpretations on the petrogenesis of granites concealing crucial information on the temporal evolution of the magma reservoirs. The construction of large composite batholiths commonly occurs over several to a dozen of million years, which requires episodic magma rejuvenations or self-similar magma replenishments (i.e., intrusion of more silicic magma) to prevent the reservoir from fully solidification (Claiborne et al., 2006; Coleman et al., 2004; Karakas et al., 2017; Memeti et al., 2022; Schaltegger et al., 2019). It is worth noting that whether these pulses of magma share the same composition and genesis remains ambiguous. Some magmatic systems may have consistent geochemistry across pulses of magma recharge (e.g., Coleman et al., 2012), while other systems show significant differences in both whole-rock geochemistry and mineral chemistry through time (e.g., Gaynor et al., 2023). Accordingly, we should firstly separate out different magma pulses which may possibly correspond to different magma sources and evolutionary processes before pondering on the petrogenesis of the whole batholith. This requires comprehensive sampling and dating analyses throughout the batholith to determine the main magmatic episodes and deal with them separately.

As for the Quxu batholith, previous studies attributed the host granitoids and MMEs either to cogenetic magmas sharing a common source at different evolution stages (e.g., Ji et al., 2009), or to magma mixing between crust- and mantle-derived melts (e.g., Ma et al., 2017; Wang et al., 2019; Wen et al., 2008). To simplify the discussion, we deem that the source nature exerts the first-order control on the composition of igneous rocks (e.g., Gao et al., 2016; Moyen and Laurent, 2018; Pearce et al., 1984). As presented in Fig. 7a, the inferred sources for the host granitoids and associated mafic–intermediate rocks gradually changed with time. Significantly, the sources for the 42–40 Ma host granitoids changed dramatically with a significant contribution of supracrustal materials as evidenced by the elevated Th/La (>1.5) and Th/Ce (>1.0) ratios (Fig. 7b and c) (Plank, 2005; Wang et al., 2006; Yang et al., 2021) and increased incorporation of HIE (e.g., Th, Rb, Pb) into the source region (Table S6 in the Appendix A). A similar scenario took place in the 42–40 Ma mafic rocks with elevated Th/Yb (>30) and relatively constant Ba/La (1–5) and Sr/Nd (2−10) ratios, which together suggest substantial incorporation of sediments into the source region (Fig. 7d–f). Additionally, the zircon oxygen and whole-rock Sr-Nd isotopic features further corroborate the progressive involvement of enriched supracrustal materials into the source region (Figs. 8 and 9). The zircon $\delta^{18}O$ and whole-rock $(^{87}Sr/^{86}Sr)_i$ fluctuatedly increased from 5.6‰ ± 0.1‰ (2σ) to 6.8‰ ± 0.1‰ (2σ) and from 0.7038 to 0.7085, respectively, while the whole-rock $\varepsilon_{Nd}(t)$ values decreased from +5.2 to −2.4 with time. Moreover, previous studies (e.g., Gurong, Kanga-gang, Kailas; Wang et al., 2014, 2015; Shui et al., 2021) reported the presence of granitic rocks of similar age (~43 Ma) that contain enriched isotopic components from the Gangdese magmatic belt. These enrichments were also described by Zhu et al. (2023) to reflect the incorporation of ancient Th-rich Indian continental materials (Ma et al., 2018). Thus, the source nature of the Quxu batholith varied with temporal and tectonic evolution, which needs more elaborate evaluations.

The differentiation of magma reservoirs might also take place apart from magma mixing. The differentiation sequence of the ~51–49 Ma group granitoids (can be roughly attributed into single episode of magma recharge) from intermediate to felsic rocks, the dark zircon rims enriched in Th and U (Miller et al., 2007) and the pronounced reduction of zircon Th/U and Zr/Hf ratios (Fig. 6c and d; Claiborne et al., 2006; Kirkland et al., 2015) in the ~42–40 Ma rocks together hint at the fractionation of magma reservoir. In addition, the xenocryst cores of Type III zircon grains (Fig. 5a) suggest the role of assimilation with the evolution of the Quxu batholith. From the analyses above, the incremental amalgamation of Quxu batholith was accompanied with complex mechanisms of crystal fractionation and wall-rock contamination.

We do not intend to inquire into the particular source nature corresponding to every episode of the magma increments in this contribution. We would like to point out the significance of pre-evaluation on the lifetime of the batholith and the discrepancy of individual magma pulse before deciphering the genesis of incrementally assembled magma reservoirs. The formation and temporal evolution of the Quxu magma reservoir are complicated with regard to the synergy of several petrogenetic mechanisms through the lifetime, which requires careful assessments.

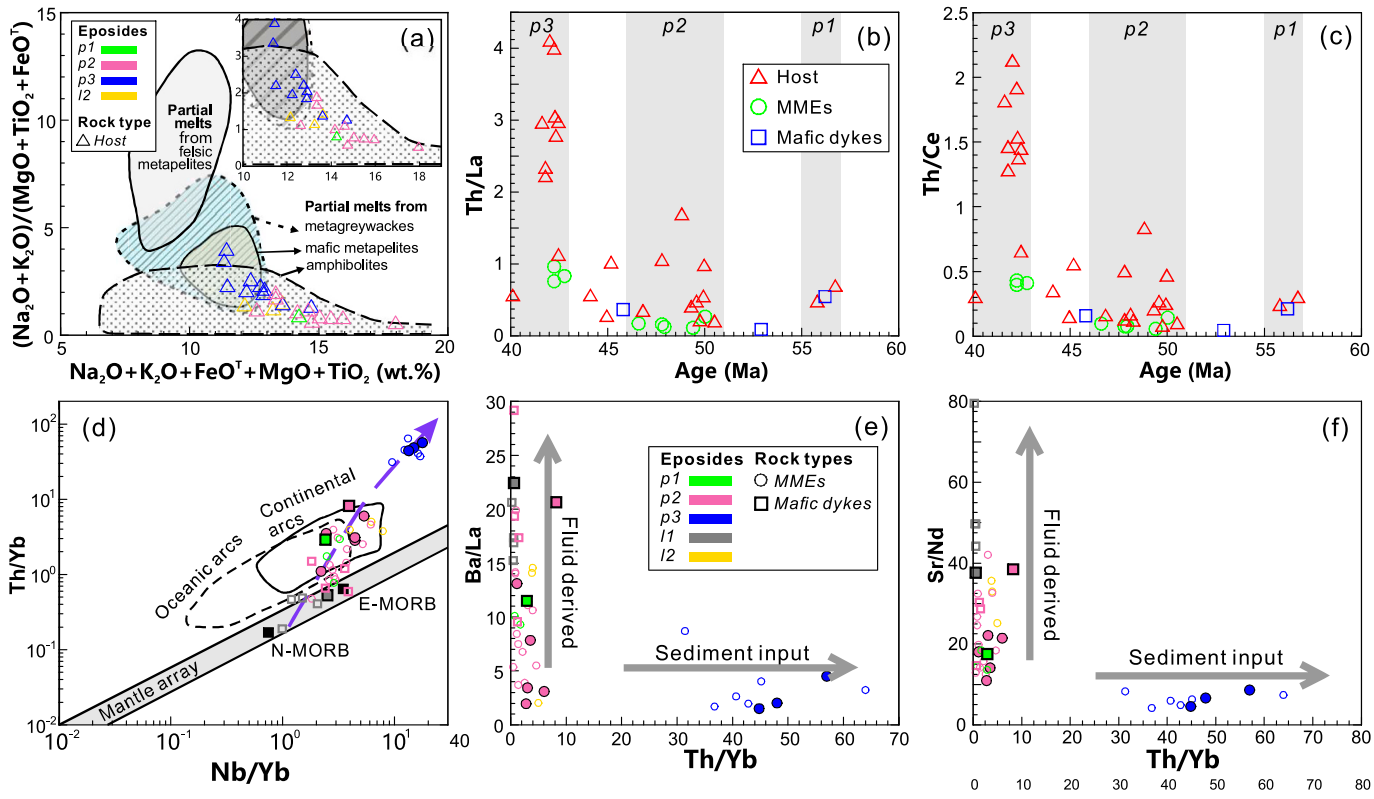

Fig. 7. Plots of whole-rock geochemical variations of the host granitoids and mafic rocks. (a) $(Na_2O + K_2O)/(MgO + TiO_2 + FeO^T)$ versus $Na_2O + K_2O + MgO + TiO_2 + FeO^T$ diagram for indicating the source rocks for the host granitoids. To avoid significant crystal fractionation, the granitoid samples with $SiO_2 > 70$ wt% were ruled out. The episodes (*p1*, *p2*, *p3* and *l1*) can refer to the text. (b) Th/La versus rock age diagram for the host granitoids. (c) Th/Ce versus rock age diagram for the host granitoids. The legends are as for Fig.7b. (d) Th/Yb versus Nb/Yb diagram for implying the source regions of the mafic rocks. The legends are as for (e). The filled shapes are from this study, while the empty shapes are from the previous studies (Ma et al., 2017; Mo et al., 2005; Wang et al., 2019; Wen et al., 2008). (e) Ba/La versus Th/Yb diagram for the mafic rocks. (f) Sr/Nd versus Th/Yb diagram for the mafic rocks. The legends are as for (e).

5.4. Temporal evolution of the Quxu batholith recorded by zircon

Zircon, as a ubiquitous accessary phase in intermediate–felsic igneous rocks, can survive through most metamorphic, weathering and reheating events and record significant information on the evolution and conditions of a magma reservoir due to its refractory nature of low diffusivities and slow growth and dissolution (Claiborne et al., 2010; Hoskin and Schaltegger, 2003; Moyen et al., 2021).

As illustrated from Fig. 6a, the magma temperatures inferred from Ti concentration in zircon ($T_{Ti\text{-}Zrn}$) show fluctuating variations with time. On the whole, $T_{Ti\text{-}Zrn}$ chronicles a protracted history of magma temperature with several rises and falls, but almost kept above or near to the granite solidus inferred from precious studies (e.g., Ackerson et al., 2018; Tuttle and Bowen, 1958). Meanwhile, the temperatures of mafic magmas are similar to those of granitic magmas and share identical tendency, which might be ascribed to the late crystallization of zircon in Zr-undersaturated status of hot mafic melts. Looking dynamically into different time intervals, the calculated magma temperature results show an overall upward trend from 60 Ma to 52 Ma, with a lesser extent of cooling in the period of 57–54 Ma. The magma temperatures reached to the highest level of 900 °C at ~52 Ma, which is approximately synchronous with the break-off of the Neo-Tethyan slab (~53 Ma; Wen et al., 2008; Zhu et al., 2022). Then the temperature decreased monotonically with a reduction of ~250 °C until ~47 Ma. From ~47 Ma to ~43 Ma, the calculated magma temperatures increased slightly by 80 °C. There was another monotonic decline of temperature starting from ~43 Ma until the consolidation of the Quxu batholith. The rises of magma temperatures could shed light on the protracted inputs of hotter magmas to the reservoir, as suggested by Claiborne et al. (2010) for the case of Spirit Mountain batholith, Nevada.

The magma redox states calculated from zircon trace elements (Loucks et al., 2020) exhibit a limited fluctuation through the lifetime of the Quxu batholith (Fig. 6b). The host granitoid melts are overall more oxidized than the mafic melts as shown by the f_{O_2}. The f_{O_2} decreased a bit from ~60 Ma to ~50 Ma with a small rise at ~51 Ma, and pointed to a relatively oxidized condition (ΔFMQ to ΔFMQ +1). From ~50 Ma to ~47 Ma, the f_{O_2} monotonically increased to ΔFMQ +2.5 at most. From ~47 Ma to the end, the f_{O_2} of the host granitoids and MMEs declined gently and finally settled at around ΔFMQ +0.5, whereas the contemporaneous f_{O_2} of mafic dykes approached to ΔFMQ – 0.5. Farner and Lee (2017) proposed that higher oxygen fugacity in magmas may reflect a thickened crust. Recent studies refer the oxidation in arc magmas to the deep accumulation and shallow segregation of hornblende (Zhang et al., 2022) or the fractionation of residual garnet (Tang et al., 2018). These two phases prefer Fe^{2+} over Fe^{3+}, so the retention of these minerals in the source region modulates the melt $Fe^{3+}/\Sigma Fe$ ratio to rise and result in oxidation. Specifically, the residual garnet retained in deep crust (>40 km) was supposed to exert the first-order control on the redox state of arc magmas, which gives rise to exceedingly increases of magma f_{O_2} values and may provide valuable clues about crustal thickening during continental collision (Tang et al., 2019, 2020b).

Zircon Zr/Hf and Th/U ratios have been widely applied to track the evolution of magmas (e.g., Bell and Kirkpatrick, 2021; Claiborne et al., 2006, 2010; Kirkland et al., 2015). Owing to the zircon's preference of Zr over Hf, the effective fractionation of zircon and coexisting mineral assemblage from liquids tends to decrease the Zr/Hf of subsequent zircon. The low zircon Zr/Hf is thus regarded as the proxy for fractional crystallization (e.g., Bell and Kirkpatrick, 2021; Claiborne et al., 2006). Th acts more incompatibly than U when incorporating into zircon through the magmatic differentiation process and thus low Th/U of

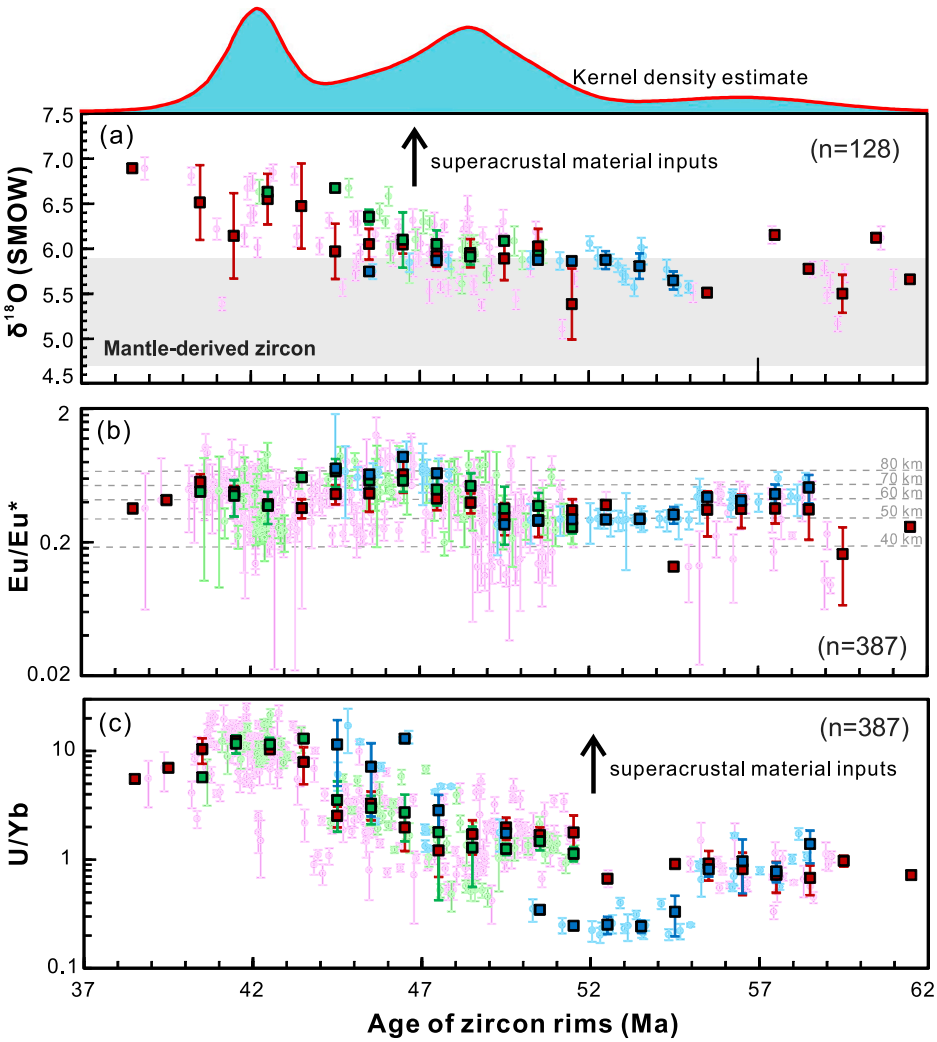

Fig. 8. Compositional changes with time in a bin of 1 Myr (2SE). (a) Zircon $\delta^{18}O$. (b) Zircon Eu/Eu* indicating the melting depth and crustal thickness, following the formula of Tang et al. (2020a). (c) Zircon U/Yb.

zircon is regarded as the indicator for crystal fractionation (e.g., Bell and Kirkpatrick, 2021; Claiborne et al., 2010; Kirkland et al., 2015; Lu et al., 2023). From ~60 Ma to ~52 Ma, the magmatic zircon of the Quxu batholith recorded an initial reduction followed by a rapid increase of Zr/Hf at ~55 Ma (Fig. 6c), corresponding to the variation of magma temperature and potential hot magma input (Fig. 6a). Then the zircon Zr/Hf ratios almost remained above 35 until ~43 Ma. The period of ~43–38 Ma is remarked by pronounced decreases of Zr/Hf in zircon, which is also matched with the coeval decrease of magma temperature (Fig. 6a). The zircon Th/U display a limited oscillating history (Fig. 6d) compared with zircon Zr/Hf. From ~60 Ma to ~43 Ma, zircon Th/U ratios vary above 0.3 on the whole and increased up to 3.0 at ~50 Ma. Coincidentally, the ~43 Ma igneous zircon record a significant decrease of Th/U that is coupled with decreasing Ti-in-zircon temperatures (Fig. 6a) and Zr/Hf (Fig. 6c), which together suggest that zircon crystallized from cool and evolved magmas. Nonetheless, even the most evolved zircons at ~42 Ma do not fit to the highly-evolved nature (e.g., zircon Zr/Hf <30; Claiborne et al., 2006), nor does the whole-rock major and trace element compositions (e.g., Zr/Hf <26, Nb/Ta <5, Eu/Eu* <0.4; cf. Wu et al., 2017 and references therein), which demonstrate the limited evolved nature of the Quxu batholith.

Zircon $\delta^{18}O$ values present an overall upward trend with several fluctuations (Fig. 8a) for the Quxu granitoids. Zircon $\delta^{18}O$ values for the rocks older than 57 Ma are within or marginally higher than those of mantle-zircon (5.3‰ ± 0.6‰, 2σ; Valley, 2003), indicating a depleted (intracrustal) source (e.g., juvenile lower crust) for the host granitoids. From ~55 Ma to ~45 Ma, the igneous zircon of the Quxu batholith show $\delta^{18}O$ values increasing progressively from ~5.5‰ to ~6.0‰ with a conspicuous drop at ~51 Ma. This suggests that the source region of the granitoids during this period was still dominated by juvenile lower crust with minor contributions from evolved continental crust. From ~45 Ma to the cession of magmatism, the zircon $\delta^{18}O$ values of the Quxu batholith become more scattered and enriched with slight drops at ~44 Ma and ~41 Ma, implying different extents of supracrustal material incorporations into the magma sources and/or wall-rock contamination. Intriguingly, the zircon $\delta^{18}O$ values of MMEs are similar to and even higher than those of host granitoids, which suggests more ancient crustal materials have been introduced to the deeper sources where mafic magmas were generated.

The whole-rock elemental data vary with time as well. The K_2O (Fig. S3a) and total alkali ($K_2O + Na_2O$) contents (Fig. S3b) display the most conspicuous transformation among major elements. The values virtually jumble together before ~43 Ma and presents remarkable increases during ~43–40 Ma (*p3*; Fig. S3a and b), suggesting the multitudinous incorporation of K-rich materials into the source regions. The HIE abundances (e.g., Th, Pb, Rb) of the Quxu granitoids older than ~50 Ma are commonly the lowest (Table S6). From ~50 Ma, the HIE abundances become more scattered and rise slightly until ~45 Ma. Significant increases of HIE concentrations (Pb >30 ppm, Th >50 ppm) and elevated Th/La and Th/Ce ratios in felsic and mafic magmas emerged

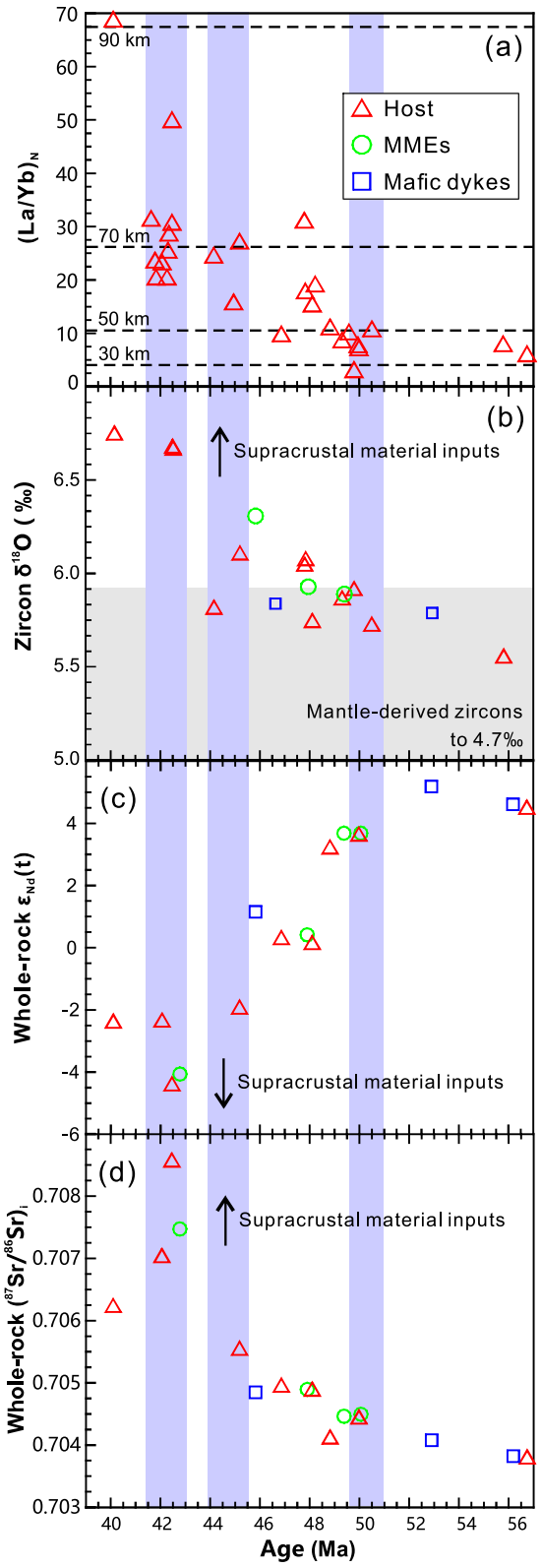

Fig. 9. The covariation of whole-rock $(La/Yb)_N$ (a), zircon $\delta^{18}O$ (b), whole-rock $\varepsilon_{Nd}(t)$ (c) and $(^{87}Sr/^{86}Sr)_i$ (d) versus rock age. The dashed lines in (a) represent melting depths calculated following the method of Profeta et al. (2015). The light purple bands denote the coordination of the above geochemical criteria and suggest obvious crustal thinning accompanied with the decreases of zircon $\delta^{18}O$ and whole-rock $(^{87}Sr/^{86}Sr)_i$ and increase of whole-rock $\varepsilon_{Nd}(t)$. (For interpretation of the references to colour in this figure legend, the reader is referred to the web version of this article.)

during ~43–40 Ma (Table S6), which are indicative of the addition of the mature upper crusts into the magma sources for the felsic rocks and the metasomatic mantle wedge possibly for the mafic magmas.

In brief, the evolution of magma physiochemical conditions and compositions inferred from zircon chemistry and whole-rock geochemistry illuminates a protracted history of the Quxu magma reservoirs. The fluctuations in magma compositions fingerprint complex petrogenic mechanisms and source nature throughout the growth history of the Quxu batholith.

5.5. The petrogenetic fingerprint of simultaneous crustal thickening and addition of crustal melts during the evolution of the Quxu batholith

Formation of granitoid batholiths is generally related either to the reworking of pre-existing crustal lithologies or minorly to the fractional crystallization of mantle-derived mafic–intermediate magmas, both of which require specific deep dynamic processes in convergent plate boundaries (Hawkesworth et al., 2010; Moyen et al., 2021). Previous studies have already identified crustal thickening in southern Tibet before and after the main collision event at ~60 Ma (Chung et al., 2009; Guo and Yang, 2023; Sundell et al., 2021; Tang et al., 2020a; Zhu et al., 2023). However, the detailed thickening processes remain poorly understood. Our data hint at the coupling of magmatic source (i.e., proportion of supracrustal materials vs. mantle-derived materials) and crustal thickness over the lifetime of the Quxu batholith.

Zircon Eu/Eu* has been applied to estimate the melting depth for intermediate–felsic rocks, owing to its roughly positive correlation with whole-rock $(La/Yb)_N$ (Tang et al., 2020a). Following this method, the Eu/Eu* of zircon grains from the Quxu batholith illustrates fluctuating changes of melting depth (Fig. 8b) and inferred episodic thickening and thinning of the crust. From ~59 Ma to ~50 Ma, the melting depth and possibly inferred crustal thickness seemed to firstly increase by ~15 km, followed a progressive reduction of ~5 km (Fig. 8b). Thereafter, rapid crustal thickening occurred between ~50–46 Ma while the crustal thickness approached ~80 km at ~46 Ma (Fig. 8b). Soon afterwards the melting depth rapidly decreased by ~25 km until 43 Ma, followed by thickening to ~15 km over the next three million years. The changes of melting depth and possible crustal thickness through the lifetime of the magma reservoirs of the Quxu batholith could reflect the episodic tectonic transitions. The short-term crustal thickening during ~59–58 Ma directly corresponds with lateral crustal shortening immediately following the initial continent–continent collision (~60 Ma; Parsons et al., 2020; Zhu et al., 2015, 2022) between Indian and Asian plates. The subsequent crustal thinning between ~58–50 Ma was also observed by previous studies (Guo and Yang, 2023; Sundell et al., 2021; Tang et al., 2020a) and it may have been triggered either by the lithospheric delamination of the Lhasa terrane (Ji et al., 2014), or by the temporal extension in response to the roll-back of subducted Neo-Tethyan slab (Zhu et al., 2015). Subsequent thickening events during ~50–46 Ma and ~43–40 were probably attributed to the ongoing collision/continent subduction. The fast decrease of crust thickness by ~25 km during ~46–43 Ma might unveil a delamination of lower crust. Continuous shortening and differentiation of continental crust could give rise to the accumulation of high-density arclogites at the root of Gangdese lower crust, which might eventually sink into the mantle (e.g., Tang et al., 2020a). The reconstruction of crustal thickness can also be achieved by using whole-rock $(La/Yb)_N$ (e.g., Profeta et al., 2015). Fig. 9 depicts an overall increasing trend of crustal thickness with pronounced thinning events during ~51–49 Ma and ~43–42 Ma, which are in agreement with the results using Eu/Eu* in zircon (Fig. 8b). The conjunction of zircon Eu/Eu* and whole-rock $(La/Yb)_N$ further validate that the process of crustal thickening is episodic rather than accomplishing at one stroke.

The incorporation of enriched crustal materials into the source region of the Quxu batholith may result in elevated U/Yb along with evolved oxygen isotope signature of zircon (e.g., Attia et al., 2020). There is a well-coordinated variation of zircon U/Yb with $\delta^{18}O$ which

shows a broadly rise from ~60 Ma to ~40 Ma with several fluctuations at around ~52 Ma, ~48 Ma, ~44 Ma and ~40 Ma (Fig. 8c). The above correlations of zircon Eu/Eu*, U/Yb and $\delta^{18}O$ (Fig. 8a–c) highlight that the deeper level at which partial melting took place, the more enriched compositions were generated and vice versa. These correlations demonstrate that the involved enriched components were melted at deeper levels during crustal thickening period, which demonstrates that the supracrustal materials were the main contributor to crustal thickening.

The whole-rock $(La/Yb)_N$ and Sr-Nd isotopes (Fig. 9) further substantiate the interpretation above. The overall ascending trend of the whole-rock $(La/Yb)_N$ (Fig. 9a) implies crustal thickening after the continent–continent collision, whereas the downward fluctuations at ~50 Ma, ~45 Ma and ~42 Ma mark crustal thinning events (also seen in Sundell et al., 2021 and Guo and Yang, 2023). As there is no observed trend of crustal contamination in any lithologies or age groups (Fig. S3e and f), the variations of Sr–Nd–O isotopes mainly reflect the evolution of source nature. The upward trends of zircon $\delta^{18}O$ (Fig. 9b) and whole-rock $(^{87}Sr/^{86}Sr)_i$ (Fig. 9c) and downward trend of whole-rock $\varepsilon_{Nd}(t)$ (Fig. 9d) record the increasing contribution of supracrustal materials to both mafic and felsic magmas. The recent synthesis on the changes in magma composition of the Gangdese magmatic belt at ~55–45 Ma has pointed out that this phenomenon is attributed to the involvement of the Indian crustal material (Zhu et al., 2023). Also, the significantly elevated

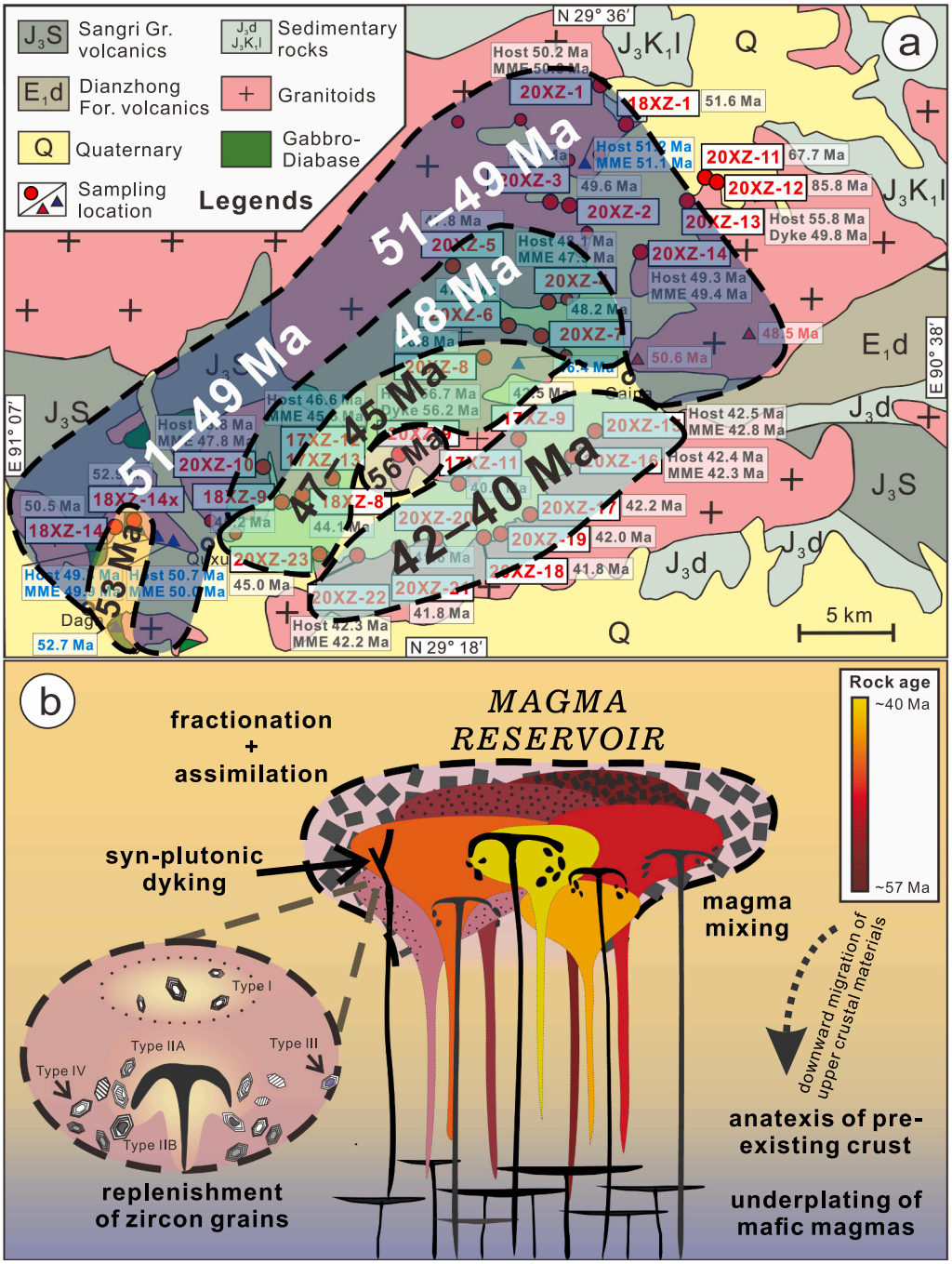

Fig. 10. A cartoon model showing the incremental amalgamation of a zoned magma reservoir of the Quxu batholith. (a) The geological map of the Quxu batholith illuminating a zoned batholith with the summative distribution of different rock ages. (b) A schematic figure illustrating the incremental growth of the Quxu magma reservoir and the replenishment of zircon grains facilitated by episodic magma recharges and hybridizations.

Th/La and Th/La of the ~43–40 Ma samples of the Quxu batholith (Fig. 7b and c) might also result from the involvement of the Th-enriched (~34 ppm) Indian middle to upper crust (Ma et al., 2018). Hence, the Indian supracrustal material is the potential candidate responsible for the enrichment of melt compositions. Conversely, the corresponding fluctuations of those geochemical proxies at the similar time during crustal thinning period [decline of whole-rock $(La/Yb)_N$] possibly originated from the relatively growing proportions of juvenile material in the source region for the Quxu composite batholith.

In short, the temporal variations of crustal thickness elucidate periodic, rather than unrelenting, processes of crustal thickening during continental collision. Although the continental collision is prone to hinder large-scale magmatism, the break-off of slab and occasional lithospheric delamination events could induce crustal thinning events and related magmatic flare-ups (Chung et al., 2009; Ji et al., 2014; Tang et al., 2020a; Zhu et al., 2022). With the thickening of continental crust, the incorporation of supracrustal materials into the source region of the Quxu granitoids appears to be more and more significant, which hints that the supracrustal components has been transported to a much deeper level and contributed a lot to crustal thickening. Consequently, the granitoids generated in different stages chronicle particular tectonic transitions, whilst the episodic growth of magma reservoir reflects the periodic transformation of deep crust.

5.6. A zoned incremental growth model for the Quxu granite batholith

To better comprehend the detailed processes of incremental amalgamation of the Quxu batholith, we synthesize the SIMS zircon U-Pb geochronologic data with petrography and sampling locations to firstly constitute a zoned granite batholith model for the Quxu batholith. As illustrated from Fig. 10a, the rock ages decrease roughly from the northwest to southeast of the batholith. The granitoids form the three main magmatism periods (~51–49 Ma, ~48–46 Ma and ~42–40 Ma) and constitute the main batholith framework with several smaller incremental magma pulses at ~56 Ma, ~53 Ma and ~45 Ma. The zoned batholith demonstrates the trend of incremental assembly and inspired us to propose a zoned incremental growth model for the formation of the Quxu batholith.

As shown in Fig. 10b, the underplating of mantle-derived mafic magmas released heat and volatiles to facilitate the partial melting of juvenile lower crustal components. The resultant intermediate–felsic melts segregated from source region and migrated upwards due to their buoyancy, and eventually were emplaced in the upper crust to form the primary magma reservoir. Meanwhile, the contemporaneous mafic magmas intruded into the reservoir and stirred and hybridized with the felsic crystal mushes. The earlier crystallized minerals (e.g., zircon, plagioclase) in the host magmas would be replenished and experienced regrowth, whereas the mafic magmas would form MMEs and *syn*-plutonic dykes after rapid quenching during mingling. With the continuous crustal thickening, the downward migration of evolved crustal components (e.g., Hines et al., 2018) and the subducted ancient Indian crustal materials (e.g., Ma et al., 2018; Zhu et al., 2022, 2023) were incorporated into the deeper source region and then gave rise to the more enriched composition of the host granitoids. Simultaneously, the magma reservoir also underwent different degrees of crystal fractionation and wall-rock contamination as suggested from the reduction of zircon Ti abundances, Zr/Hf and Th/U ratios and the presence of inherited zircon cores, respectively.

In contrast to the crustal thickening, the episodes of crustal thinning would cause enhanced magmatism with hotter and more primitive features as aforementioned. The slab break-off and delamination of the lower crust root were apt to introduce the upwelling of hot asthenosphere which could provide heat to the juvenile lower crust. The resultant periodic felsic and mafic magmas then migrated upwards and contributed to the incremental amalgamation of magma reservoirs. At the final stage of incremental growth of the Quxu batholith (i.e., ~42–40 Ma), the lithospheric delamination triggered partial melting of highly metasomatic mantle (by the interaction with Indian continent) and generated shoshonitic mafic melts. Concurrently, the persistent subduction of the Indian ancient crust delivered plenty of mature components to the deep crustal level which ultimately melted to produce the high-K calc-alkaline felsic magmas. The simultaneous felsic and mafic magmas mixed together and became the last increment of the Quxu composite batholith (Fig. 10b).

6. Conclusions

The Quxu batholith with a prolonged crystallization history (ca. 16.6 Myr) provides a valuable opportunity to investigate the detailed processes of incremental growth of magma reservoirs. Inspired by the new SIMS zircon U-Pb geochronologic data, we firstly recognize a temporally and lithologically zoned batholith in the Quxu area. On the basis of careful evaluations on microstructural signature and compositional analysis of zircon and plagioclase from the host granitoids of the Quxu batholith, episodic magma recharge and hybridization are envisaged as the main contributor to the incremental amalgamation of the magma reservoir. The extra heat, volatiles and chemical turbulences resulted from the episodic injections of magma left deep imprints on both mineral and rock scales. After distinguishing the temporal variations of zircon and whole-rock compositions and Sr–Nd–O isotopes, we emphasize pre-assessments on the lifetime of large granite batholith and the geochemical discrepancy of individual magma pulse before elucidating the genesis of the whole magma reservoir. Furthermore, we identified the coordinated changes of whole-rock $(La/Yb)_N$ and Sr–Nd–O isotopes throughout the lifetime of the Quxu batholith, which demonstrates that the crustal thickening process is periodic during the tectonic transition from subduction to collision, and the incorporation of supracrustal material tends to be more significant during crustal thickening events. Finally, the incremental growth model illustrates the assemblage process of the Quxu batholith and the replenishment of zircon.

Supplementary data to this article can be found online at https://doi.org/10.1016/j.lithos.2023.107466.

Declaration of Competing Interest

The authors declare that they have no known competing financial interests or personal relationships that could have appeared to influence the work reported in this paper.

Acknowledgements

We thank Wen-Li Xie and Lan-Lan Tian (NJU) for SIMS analysis, Shuang Xu and Teng-Da Guo (Shandong Bureau) for EMPA analysis, Qiu-Yun Yuan and Jun Du (Hongchuang Ltd.) for whole-rock Sr-Nd isotope and LA–ICP–MS plagioclase trace element analyses. We are grateful to Sean Gaynor and Blake Wallrich for their efforts on improving the quality of the original manuscript and to Olivier Bachmann for the valuable discussion on this work. This work was financially supported by the National Natural Science Foundation of China (grant No. 42025202), the Frontiers Science Center for Critical Earth Material Cycling, the China Scholarship Council (grant No. 202106190127) and the State Key Laboratory for Mineral Deposits, Nanjing University.

Appendix A. Analytical methods

Back-scattered-electron (BSE) imaging, electron microprobe analysis (EMPA) and compositional mapping of plagioclase grains were conducted using a JXA-8230 (JEOL) instrument at the Testing Centre of the Shandong Bureau of China Metallurgy and Geology, Ji'nan, China. The analyses were collected under the following conditions: accelerating voltage of 15 kV, beam current of 2.0×10^{-8} A. Beam size of 10 μm was

applied for EMPA, and interval of 1.5 μm × 1.5 μm with dwell time of 20 ms was taken for compositional mapping. The determination of in situ plagioclase trace element abundances was conducted using a LA–ICP–MS instrument at Nanjing Hongchuang Geological Exploration Technology Service Co., Ltd. The Resolution SE model (Applied Spectra) laser ablation system was attached to an Agilent 7900 ICP–MS instrument. Thin sections were fixed onto the sample holder and cleaned prior to the analysis using analytical reagent grade methanol. Pre-analysis ablation was conducted for each spot analysis using 5 laser shots (~1 μm in depth) to remove potential surface contamination. The analysis was performed using 37 μm diameter spot at 10 Hz and a fluence of 4 J/cm^2. NIST 610 was used as primary reference material, while BCR-2G and BIR-1G were used as secondary reference material. Triplets of reference material were bracketed between multiple groups of 10 to 12 unknown samples. The EMPA determined ^{43}Ca content was used as internal standard element to calibrate trace element concentrations.

Zircon crystals were selected following reflected and transmitted light photomicrographs as well as cathodoluminescence (CL) imaging. SIMS in situ zircon U-Pb isotopic dating and trace element analyses were carried out using a newly-installed IMS (ion microscope) 1300-HR^3 (CAMECA) ion microprobe at the State Key Laboratory for Mineral Deposits Research, Nanjing University (MiDeR-NJU). In this study, the results include the concordia age, the concentrations of Ti and REE elements and Th/U ratios, acquired by a single analytical spot with beam size of 10 μm. A 5 nA, −13 kV O^- Gaussian beam was subjected to impact on the golden surface of zircon grains. The +10 kV positive secondary ions travelled through the instrument and were detected by the electron multipliers on the Mono-collection and the Multi-collection with a peak-hopping sequence. A mass resolution >15,000 (M/ΔM) was utilized on the Mono-collection. The mass resolution 8000 (M/ΔM) set at the Multi-collections was sufficient for the U-Pb dating. Each analysis contains an 80 s pre-sputtering to remove the Au-coating, a beam centering at the Field Aperture and Contrast Aperture, an optimization on Energy Slit, a mass calibration at $^{90}Zr_2^{16}O^+$ peak and 5 cycles of the whole analysis sequence (Table S8). Oxygen flooding at 4×10^{-6} mbar was applied on all of these analyses. Zircon standards Plešovice and Qinghu were used as external standard to monitor U-Pb dating analytical precision, while the trace element abundances were calibrated to the standard 91,500. To avoid potential chemical disturbances induced by post-magmatic alteration (Hoskin, 2005; Laurent et al., 2021), we set the criterion for "pristine zircon" of measured La concentration < 0.2 ppm as indicated from Zou et al. (2019) and dismissed the analyses that miss this criterion. The analysis sequence of the SIMS U-Pb isotopes and trace elements method is summarized in Table S8.

Following U-Pb dating and trace element analysis, the dated zircon grains were further analysed for in situ zircon oxygen isotopes using the same IMS 1300-HR^3 ion microprobe. The oxygen isotope analyses were determined on the same spots or similar domains as for SIMS zircon U-Pb dating analysis. A primary $^{133}Cs^+$ ion beam (2.8–3 nA current and 20 keV total impact energy) was focused on the zircon surface. A 20 μm × 20 μm raster was used in this study, and a normal-incidence electron gun was used for charge compensation. A NMR field sensor was applied to stabilize the magnetic field. The signals of ^{16}O and ^{18}O were collected simultaneously using two Faraday cups at positions of L'2 and H′2, respectively. The L'2 and H′2 positions were configured with a resistor circuit of 10^{10} Ω and 10^{11} Ω, respectively. The mass resolving power (MRP, M/ΔM), measured at 50% peak height, was set at ~2400 to minimize isobaric interferences. The total analytical time was about 4.5 min per pit: 100 s pre-sputtering (to remove the Au coating), ~60 s automatic centering of the secondary ions in the field aperture, and a total of 80 s integration of secondary ions (twenty cycles × 4 s). The counting rate of ^{16}O was approximately 2.9×10^9–3.2×10^9 cps. Zircon standards Penglai and Qinghu were used as external standards for quality control.

Whole-rock major and trace element analyses were also performed at MiDeR-NJU. Major elements were acquired using an ARL9900 (Thermo Fisher Scientific) X-Ray fluorescence spectrometer. United States Geological Survey (USGS) reference materials RGM-2, BHVO-2 and BCR-2 were used for quality control. The analytical precision is generally better than 2% for most elements. Trace elements were analysed in solution after acid digestion using an Aurora M90 (Analytik Jena) ICP–MS instrument, with USGS standards BHVO-2, AGV-2, and W-2 used for quality control. The analytical precision is generally better than 5% for most elements.

Bulk-rock Rb-Sr and Sm-Nd isotopic analyses were achieved by a Neptune Plus (Thermo Fisher Scientific) multiple collector (MC)–ICP–MS at Nanjing Hongchuang Geological Exploration Technology Service Co., Ltd. The mass fractionation of measured $^{87}Sr/^{86}Sr$ and $^{143}Nd/^{144}Nd$ was corrected by normalizing to $^{86}Sr/^{88}Sr = 0.1194$ and $^{146}Nd/^{144}Nd = 0.7219$, respectively. Drift of instrument was corrected using NIST SRM 987 and JNdi-1 standards as external standards for Rb-Sr and Sm-Nd isotopic analyses, respectively. $^{87}Rb/^{86}Sr$ and $^{147}Sm/^{143}Nd$ were calculated using whole-rock Rb/Sr and Sm/Nd and related natural abundances and atomic weights. USGS reference materials BCR-2, BHVO-2, and AVG-2 were analysed to monitor the analytical quality. Isotope ratios were corrected to initial values applying element concentrations previously obtained by ICP–MS and crystallization ages obtained by SIMS zircon U-Pb dating.

References

Ackerson, M.R., Mysen, B.O., Tailby, N.D., Watson, E.B., 2018. Low-temperature crystallization of granites and the implications for crustal magmatism. Nature 559, 94–97. https://doi.org/10.1038/s41586-018-0264-2.

Annen, C., Blundy, J.D., Sparks, R.S.J., 2006. The genesis of intermediate and silicic magmas in deep crustal hot zones. J. Petrol. 47, 505–539. https://doi.org/10.1093/petrology/egi084.

Attia, S., Cottle, J.M., Paterson, S.R., 2020. Erupted zircon record of continental crust formation during mantle driven arc flare-ups. Geology 48, 446–451. https://doi.org/10.1130/g46991.1.

Baxter, S., Feely, M., 2002. Magma mixing and mingling textures in granitoids: examples from the Galway Granite, Connemara, Ireland. Mineral. Petrol. 76, 63–74. https://doi.org/10.1007/s0071000101788.

Bell, E.A., Kirkpatrick, H.M., 2021. Effects of crustal assimilation and magma mixing on zircon trace element relationships across the Peninsular Ranges Batholith. Chem. Geol. 586, 120616 https://doi.org/10.1016/j.chemgeo.2021.120616.

Bindeman, I.N., Melnik, O.E., 2016. Zircon survival, rebirth and recycling during crustal melting, magma crystallization, and mixing based on numerical modelling. J. Petrol. 57, 437–460. https://doi.org/10.1093/petrology/egw013.

Blundy, J.D., Wood, B.J., 1991. Crystal-chemical controls on the partitioning of Sr and Ba between plagioclase feldspar, silicate melts, and hydrothermal solutions. Geochim. Cosmochim. Acta 55, 193–209. https://doi.org/10.1016/0016-7037(91)90411-w.

Browne, B.L., Eichelberger, J.C., Patino, L.C., Vogel, T.A., Uto, K., Hoshizumi, H., 2006. Magma mingling as indicated by texture and Sr/Ba ratios of plagioclase phenocrysts from Unzen volcano, SW Japan. J. Volcanol. Geotherm. Res. 154, 103–116. https://doi.org/10.1016/j.jvolgeores.2005.09.022.

Campbell, I.H., Taylor, S.R., 1983. No water, no granites – no oceans, no continents. Geophys. Res. Lett. 10, 1061–1064. https://doi.org/10.1029/GL010i011p01061.

Castro, A., 2001. Plagioclase morphologies in assimilation experiments: implications for disequilibrium melting in the generation of granodiorite rocks. Mineral. Petrol. 71, 31–49. https://doi.org/10.1007/s007100170044.

Chung, S.L., Chu, M.F., Ji, J.Q., O'Reilly, S.Y., Pearson, N.J., Liu, D.Y., Lee, T.Y., Lo, C.H., 2009. The nature and timing of crustal thickening in Southern Tibet: Geochemical and zircon Hf isotopic constraints from postcollisional adakites. Tectonophysics 477, 36–48. https://doi.org/10.1016/j.tecto.2009.08.008.

Claiborne, L.L., Miller, C.F., Walker, B.A., Wooden, J.L., Mazdab, F.K., Bea, F., 2006. Tracking magmatic processes through Zr/Hf ratios in rocks and Hf and Ti zoning in zircons: an example from the Spirit Mountain batholith, Nevada. Mineral. Mag. 70, 517–543. https://doi.org/10.1180/0026461067050348.

Claiborne, L.L., Miller, C.F., Flanagan, D.M., Clynne, M.A., Wooden, J.L., 2010. Zircon reveals protracted magma storage and recycling beneath Mount St. Helens. Geology 38, 1011–1014. https://doi.org/10.1130/g31285.1.

Coleman, D.S., Gray, W., Glazner, A.F., 2004. Rethinking the emplacement and evolution of zoned plutons: geochronologic evidence for incremental assembly of the Tuolumne Intrusive Suite. Calif. Geol. 32, 433. https://doi.org/10.1130/g20220.1.

Coleman, D., Bartley, J.M., Glazner, A.F., Pardue, M.J., 2012. Is chemical zonation in plutonic rocks driven by changes in source magma composition or shallow-crustal differentiation? Geosphere 8, 1568–1587. https://doi.org/10.1130/ges00798.1.

Coote, A.C., Shane, P., 2016. Crystal origins and magmatic system beneath Ngauruhoe volcano (New Zealand) revealed by plagioclase textures and compositions. Lithos 260, 107–119. https://doi.org/10.1016/j.lithos.2016.05.017.

Farner, M.J., Lee, C.-T.A., 2017. Effects of crustal thickness on magmatic differentiation in subduction zone volcanism: a global study. Earth Planet. Sci. Lett. 470, 96–107. https://doi.org/10.1016/j.epsl.2017.04.025.

Ferry, J.M., Watson, E.B., 2007. New thermodynamic models and revised calibrations for the Ti-in-zircon and Zr-in-rutile thermometers. Contrib. Mineral. Petrol. 154, 429–437. https://doi.org/10.1007/s00410-007-0201-0.

Gao, P., Zheng, Y.F., Zhao, Z.F., 2016. Distinction between S-type and peraluminous I-type granites: Zircon versus whole-rock geochemistry. Lithos 258–259, 77–91. https://doi.org/10.1016/j.lithos.2016.04.019.

Gaynor, S.P., Smith, T.M., Schaltegger, U., 2023. Tracing magmatic genesis and evolution through single zircon crystals from successive supereruptions from the Socorro Caldera complex, USA. Earth Planet. Sci. Lett. 616, 118236 https://doi.org/10.1016/j.epsl.2023.118236.

Glazner, A.F., Bartley, J.M., Coleman, D.S., Gray, W., Taylor, R.Z., 2004. Are plutons assembled over millions of years by amalgamation from small magma chambers? Geol. Soc. Am. Today 14, 4. https://doi.org/10.1130/1052-5173(2004)014<0004:apaomo>2.0.co;2.

Grove, T.L., Baker, M.B., Kinzler, R.J., 1984. Coupled CaAl–NaSi diffusion in plagioclase feldspar: experiments and applications to cooling rate speedometry. Geochim. Cosmochim. Acta 48, 2113–2121. https://doi.org/10.1016/0016-7037(84)90391-0.

Guo, P., Yang, T., 2023. Quantifying continental crust thickness using the machine learning method. J. Geophys. Res. Solid Earth 128. https://doi.org/10.1029/2022jb025970.

Hawkesworth, C.J., Dhuime, B., Pietranik, A.B., Cawood, P.A., Kemp, A.I.S., Storey, C.D., 2010. The generation and evolution of the continental crust. J. Geol. Soc. Lond. 167, 229–248. https://doi.org/10.1144/0016-76492009-072.

Hines, R., Paterson, S.R., Memeti, V., Chambers, J.A., 2018. Nested incremental growth of zoned upper crustal plutons in the Southern Uplands Terrane, UK: fractionating, mixing, and contaminated magma fingers. J. Petrol. 59, 483–516. https://doi.org/10.1093/petrology/egy034.

Hoskin, P.W.O., 2005. Trace-element composition of hydrothermal zircon and the alteration of Hadean zircon from the Jack Hills, Australia. Geochim. Cosmochim. Acta 69, 637–648. https://doi.org/10.1016/j.gca.2004.07.006.

Hoskin, P.W.O., Schaltegger, U., 2003. The composition of zircon and igneous and metamorphic petrogenesis. Rev. Mineral. Geochem. 53, 27–62. https://doi.org/10.2113/0530027.

Ji, W.-Q., Wu, F.-Y., Chung, S.-L., Li, J.-X., Liu, C.-Z., 2009. Zircon U–Pb geochronology and Hf isotopic constraints on petrogenesis of the Gangdese batholith, southern Tibet. Chem. Geol. 262, 229–245. https://doi.org/10.1016/j.chemgeo.2009.01.020.

Ji, W.-Q., Wu, F.-Y., Chung, S.-L., Liu, C.-Z., 2014. The Gangdese magmatic constraints on a latest cretaceous lithospheric delamination of the Lhasa terrane, southern Tibet. Lithos 210–211, 168–180. https://doi.org/10.1016/j.lithos.2014.10.001.

Jiang, C.-H., Wang, D., Du, D.-H., Wang, X.-L., 2023. Estimation of an ephemeral cooling for silicic magma reservoirs using thermal simulation. J. Asian Earth Sci. 241, 105442 https://doi.org/10.1016/j.jseaes.2022.105442.

Karakas, O., Degruyter, W., Bachmann, O., Dufek, J., 2017. Lifetime and size of shallow magma bodies controlled by crustal-scale magmatism. Nat. Geosci. 10, 446–450. https://doi.org/10.1038/ngeo2959.

Kirkland, C.L., Smithies, R.H., Taylor, R.J.M., Evans, N., McDonald, B., 2015. Zircon Th/U ratios in magmatic environs. Lithos 212–215, 397–414. https://doi.org/10.1016/j.lithos.2014.11.021.

Laurent, O., Moyen, J.-F., Wotzlaw, J.-F., Björnsen, J., Bachmann, O., 2021. Early Earth zircons formed in residual granitic melts produced by tonalite differentiation. Geology 50, 437–441. https://doi.org/10.1130/g49232.1.

Loucks, R.R., Fiorentini, M.L., Henríquez, G.J., 2020. New magmatic oxybarometer using trace elements in zircon. J. Petrol. 61, egaa034. https://doi.org/10.1093/petrology/egaa034.

Lu, T.-Y., He, Z.-Y., Klemd, R., 2023. Different magma differentiation processes of post-onset collision adakitic rocks in the Gangdese Batholith: evidence from zircon trace elements. Chem. Geol. 620, 121345 https://doi.org/10.1016/j.chemgeo.2023.121345.

Ma, L., Wang, B.-D., Jiang, Z.-Q., Wang, Q., Li, Z.-X., Wyman, D.A., Zhao, S.-R., Yang, J.-H., Gou, G.-N., Guo, H.-F., 2014. Petrogenesis of the early Eocene adakitic rocks in the Napuri area, southern Lhasa: partial melting of thickened lower crust during slab break-off and implications for crustal thickening in southern Tibet. Lithos 196–197, 321–338. https://doi.org/10.1016/j.lithos.2014.02.011.

Ma, X., Meert, J.G., Xu, Z., Zhao, Z., 2017. Evidence of magma mixing identified in the early Eocene Caina pluton from the Gangdese Batholith, southern Tibet. Lithos 278–281, 126–139. https://doi.org/10.1016/j.lithos.2017.01.020.

Ma, L., Kerr, A.C., Wang, Q., Jiang, Z.-Q., Hu, W.-L., 2018. Early cretaceous (~140 Ma) aluminous A-type granites in the Tethyan Himalaya, Tibet: products of crust-mantle interaction during lithospheric extension. Lithos 300–301, 212–226. https://doi.org/10.1016/j.lithos.2017.11.023.

McDonough, W.F., Sun, S.S., Ringwood, A.E., Jagoutz, E., Hofmann, A.W., 1992. Potassium, rubidium, and cesium in the Earth and Moon and the evolution of the mantle of the Earth. Geochim. Cosmochim. Acta 56, 1001–1012. https://doi.org/10.1016/0016-7037(92)90043-i.

Memeti, V., Paterson, S.R., Mundil, R., 2022. Coupled magmatic and host rock processes during the initiation of the Tuolumne Intrusive complex, Sierra Nevada, California, USA: a transition from ephemeral sheets to long-lived, active magma mushes. Geol. Soc. Am. Bull. 134, 1347–1374. https://doi.org/10.1130/b35871.1.

Miller, J.S., Matzel, J.E.P., Miller, C.F., Burgess, S.D., Miller, R.B., 2007. Zircon growth and recycling during the assembly of large, composite arc plutons. J. Volcanol. Geotherm. Res. 167, 282–299. https://doi.org/10.1016/j.jvolgeores.2007.04.019.

Mo, X.X., Dong, G.C., Zhao, Z.D., Zhou, S., Wang, L.L., Qiu, R.Z., Zhang, F.Q., 2005. Spatial and temporal distribution and characteristics of granitoids in the Gangdese, Tibet and implication for crustal growth and evolution. Geol. J. China Univ. 11, 281–290 (in Chinese with English abstract).

Moyen, J.-F., Laurent, O., 2018. Archaean tectonic systems: a view from igneous rocks. Lithos 302–303, 99–125. https://doi.org/10.1016/j.lithos.2017.11.038.

Moyen, J.-F., Janoušek, V., Laurent, O., Bachmann, O., Jacob, J.-B., Farina, F., Fiannacca, P., Villaros, A., 2021. Crustal melting vs. fractionation of basaltic magmas: Part 1, granites and paradigms. Lithos 402–403, 106291. https://doi.org/10.1016/j.lithos.2021.106291.

Parsons, A.J., Hosseini, K., Palin, R.M., Sigloch, K., 2020. Geological, geophysical and plate kinematic constraints for models of the India-Asia collision and the post-Triassic central Tethys oceans. Earth Sci. Rev. 208, 103084 https://doi.org/10.1016/j.earscirev.2020.103084.

Pearce, J.A., Harris, N.B.W., Tindle, A.G., 1984. Trace element discrimination diagrams for the tectonic interpretation of granitic rocks. J. Petrol. 25, 956–983. https://doi.org/10.1093/petrology/25.4.956.

Pietranik, A., Koepke, J., 2014. Plagioclase transfer from a host granodiorite to mafic microgranular enclaves: Diverse records of magma mixing. Mineral. Petrol. 108, 681–694. https://doi.org/10.1007/s00710-014-0326-6.

Plank, T., 2005. Constraints from thorium/lanthanum on sediment recycling at subduction zones and the evolution of the continents. J. Petrol. 46, 921–944. https://doi.org/10.1093/petrology/egi005.

Profeta, L., Ducea, M.N., Chapman, J.B., Paterson, S.R., Gonzales, S.M.H., Kirsch, M., Petrescu, L., DeCelles, P.G., 2015. Quantifying crustal thickness over time in magmatic arcs. Sci. Rep. 5 https://doi.org/10.1038/srep17786.

Ruan, B., Luo, B., Zhang, H., Guo, L., Xu, W., Zhao, X., Zhang, W., Guo, J., 2019. Magma mixing of the Eocene Quxu batholith from the Gangdese magmatic belt, South Tibet: evidence from cathodoluminescence characteristics and composition changes of plagioclase. Earth Sci. 44, 1834–1848 (in Chinese with English abstract). https://doi.org/10.3799/dqkx.2018.397.

Scaillet, B., Evans, B.W., 1999. The 15 June 1991 eruption of Mount Pinatubo. I. Phase equilibria and pre-eruption P–T–f_{O2}–f_{H2O} conditions of the dacite magma. J. Petrol. 40, 381–411. https://doi.org/10.1093/petroj/40.3.381.

Schaltegger, U., Nowak, A., Ulianov, A., Fisher, C.M., Gerdes, A., Spikings, R., Whitehouse, M.J., Bindeman, I., Hanchar, J.M., Duff, J., Vervoort, J.D., Sheldrake, T., Caricchi, L., Brack, P., Müntener, O., 2019. Zircon petrochronology and $^{40}Ar/^{39}Ar$ thermochronology of the Adamello Intrusive Suite, N. Italy: monitoring the growth and decay of an incrementally assembled magmatic system. J. Petrol. 60, 701–722. https://doi.org/10.1093/petrology/egz010.

Schärer, U., Xu, R.-H., Allègre, C.J., 1984. U–Pb geochronology of Gangdese (Transhimalaya) plutonism in the Lhasa–Xigaze region, Tibet. Earth Planet. Sci. Lett. 69, 311–320. https://doi.org/10.1016/0012-821x(84)90190-0.

Shui, X.-F., Klemd, R., He, Z.-Y., Mao, J.-W., Zhao, Y.-Y., 2021. Geochronology and petrogenesis of Eocene gabbros and granitic rocks of the eastern Gangdese belt, southern Tibet: implications for the timing of India–Asia collision. Gondwana Res. 97, 145–157. https://doi.org/10.1016/j.gr.2021.05.019.

Singer, B.S., Pearce, T.H., Kolisnik, A.M., Myers, J.D., 1993. Plagioclase zoning in mid-Pleistocene lavas from the Seguam volcanic center, central Aleutian arc, Alaska. Am. Mineral. 78, 143–157.

Sun, S.S., McDonough, W.F., 1989. Chemical and isotopic systematics of oceanic basalts: implications for mantle composition and processes. Geol. Soc. Lond. Spec. Publ. 42, 313–345. https://doi.org/10.1144/gsl.sp.1989.042.01.19.

Sundell, K., Laskowski, A., Kapp, P., Ducea, M., Chapman, J., 2021. Jurassic to Neogene quantitative crustal thickness estimates in southern Tibet. Geol. Soc. Am. Today 31, 4–10. https://doi.org/10.1130/Geological Society of Americatg461a.1.

Tang, M., Erdman, M., Eldridge, G., Lee, C.-T.A., 2018. The redox "filter" beneath magmatic orogens and the formation of continental crust. Sci. Adv. 4 https://doi.org/10.1126/sciadv.aar4444.

Tang, M., Lee, C.-T.A., Costin, G., Höfer, H.E., 2019. Recycling reduced iron at the base of magmatic orogens. Earth Planet. Sci. Lett. 528, 115827 https://doi.org/10.1016/j.epsl.2019.115827.

Tang, M., Ji, W.-Q., Chu, X., Wu, A., Chen, C., 2020a. Reconstructing crustal thickness evolution from europium anomalies in detrital zircons. Geology 49, 76–80. https://doi.org/10.1130/g47745.1.

Tang, M., Lee, C.-T.A., Ji, W.-Q., Wang, R., Costin, G., 2020b. Crustal thickening and endogenic oxidation of magmatic sulfur. Sci. Adv. 6 https://doi.org/10.1126/sciadv.aba6342.

Tuttle, O.F., Bowen, N.L., 1958. Origin of granite in the light of experimental studies in the system $NaAlSi_3O_8$–$KAlSi_3O_8$–SiO_2–H_2O. Geol. Soc. Am. Memoir 74, 1–146. https://doi.org/10.1130/MEM74-p1.

Valley, J.W., 2003. Oxygen isotopes in zircon. Rev. Mineral. Geochem. 53, 343–385. https://doi.org/10.2113/0530343.

Wang, Q., Xu, J.-F., Jian, P., Bao, Z.-W., Zhao, Z.-H., Li, C.-F., Xiong, X.-L., Ma, J.-L., 2006. Petrogenesis of adakitic porphyries in an extensional tectonic setting, Dexing, South China: implications for the genesis of porphyry copper mineralization. J. Petrol. 47, 119–144. https://doi.org/10.1093/petrology/egi070.

Wang, R., Richards, J.P., Hou, Z., Yang, Z., DuFrane, S.A., 2014. Increased magmatic water content—the key to Oligo-Miocene porphyry Cu–Mo–Au formation in the eastern Gangdese Belt, Tibet. Econ. Geol. 109, 1315–1339. https://doi.org/10.2113/econgeo.109.5.1315.

Wang, Q., Zhu, D.-C., Cawood, P.A., Zhao, Z.-D., Liu, S.-A., Chung, S.-L., Zhang, L.-L., Liu, D., Zheng, Y.-C., Dai, J.-G., 2015. Eocene magmatic processes and crustal thickening in southern Tibet: insights from strongly fractionated ca. 43 Ma granites in the western Gangdese Batholith. Lithos 239, 128–141. https://doi.org/10.1016/j.lithos.2015.10.003.

Wang, R.-Q., Qiu, J.-S., Yu, S.-B., Lin, L., Xu, H., 2019. Magma mixing origin for the Quxu intrusive complex in southern Tibet: insights into the early Eocene magmatism and geodynamics of the southern Lhasa subterrane. Lithos 328–329, 14–32. https://doi.org/10.1016/j.lithos.2019.01.019.

Wang, D., Wang, X.L., Bindeman, I.N., Du, D.H., Li, J.Y., Jiang, C.H., 2021. Ephemeral magma reservoirs during the incremental growth of the Neoproterozoic Jiuling composite batholith in South China. J. Geophys. Res. Solid Earth 126. https://doi.org/10.1029/2021jb022758.

Watson, E.B., Harrison, T.M., 1983. Zircon saturation revisited: temperature and composition effects in a variety of crustal magma types. Earth and Planet. Sci. Lett. 64, 295–304. https://doi.org/10.1016/0012-821x(83)90211-x.

Wen, D., Liu, D., Chung, S., Chu, M., Ji, J., Zhang, Q., Song, B., Lee, T., Yeh, M., Lo, C., 2008. Zircon SHRIMP U–Pb ages of the Gangdese Batholith and implications for Neotethyan subduction in southern Tibet. Chem. Geol. 252, 191–201. https://doi.org/10.1016/j.chemgeo.2008.03.003.

Wu, F., Liu, X., Ji, W., Wang, J., Yang, L., 2017. Highly fractionated granites: Recognition and research. Sci. China Earth Sci. 60, 1201–1219. https://doi.org/10.1007/s11430-016-5139-1.

Yang, Z.-Y., Wang, Q., Hao, L.-L., Wyman, D.A., Ma, L., Wang, J., Qi, Y., Sun, P., Hu, W.-L., 2021. Subduction erosion and crustal material recycling indicated by adakites in Central Tibet. Geology 49, 708–712. https://doi.org/10.1130/g48486.1.

Yin, A., Harrison, T.M., 2000. Geologic evolution of the Himalayan–Tibetan orogen. Annu. Rev. Earth Planet. Sci. 28, 211–280. https://doi.org/10.1146/annurev.earth.28.1.211.

Yu, Y., Guan, Q., Woo, I., Li, Z., Jing, T., Wang, D., 2023. Petrogenesis of the Quxu intrusive complex: implications for Eocene magmatism in the southern Lhasa Terrane, Tibet. Geol. J. 58, 1727–1740. https://doi.org/10.1002/gj.4690.

Zhang, Y.-Z., Wang, X.-L., Li, J.-Y., He, Z.-Y., Zhang, F.-F., Chen, X., Wang, S., Du, D.-H., Huang, Y., Jiang, C.-H., 2021. Oligocene leucogranites of the Gangdese batholith, southern Tibet: fractional crystallization of felsic melts from juvenile lower crust. J. Petrol. 62, egab076. https://doi.org/10.1093/petrology/egab076.

Zhang, J., Wang, R., Hong, J., 2022. Amphibole fractionation and its potential redox effect on arc crust: evidence from the Kohistan arc cumulates. Am. Mineral. 107, 1779–1788. https://doi.org/10.2138/am-2022-8141.

Zhu, D.-C., Wang, Q., Zhao, Z.-D., Chung, S.-L., Cawood, P.A., Niu, Y., Liu, S.-A., Wu, F.-Y., Mo, X.-X., 2015. Magmatic record of India-Asia collision. Sci. Rep. 5 https://doi.org/10.1038/srep14289.

Zhu, D.-C., Wang, Q., Weinberg, R.F., Cawood, P.A., Chung, S.-L., Zheng, Y.-F., Zhao, Z., Hou, Z.-Q., Mo, X.-X., 2022. Interplay between oceanic subduction and continental collision in building continental crust. Nat. Commun. 13 https://doi.org/10.1038/s41467-022-34826-0.

Zhu, D.C., Wang, Q., Weinberg, R.F., Cawood, P.A., Zhao, Z.D., Hou, Z.Q., Mo, X.X., 2023. Continental crustal growth processes recorded in the Gangdese batholith, southern Tibet. Annu. Rev. Earth Planet. Sci. 51, 155–188. https://doi.org/10.1146/annurev-earth-032320-110452.

Zou, X., Qin, K., Han, X., Li, G., Evans, N.J., Li, Z., Yang, W., 2019. Insight into zircon REE oxy-barometers: a lattice strain model perspective. Earth Planet. Sci. Lett. 506, 87–96. https://doi.org/10.1016/j.epsl.2018.10.031.